Communication in Physical Sciences, 2026, 13(7):1006-1039

Mineralogical and Geochemical Characterization of Gold-Bearing Rocks in Mararaban Yauri, Northwestern Nigeria

Samaila Garba Riskuwa and Ishak Yau Tanko
Received: 2 April 2026/Accepted: 27 June 2026 /Published: 08 July 2026
https://dx.doi.org/10.4314/cps.v13i7.1

Abstract: *The Mararaban Yauri area within the Zuru Schist Belt of northwestern Nigeria hosts significant artisanal gold workings, yet the mineralogical characteristics, hydrothermal alteration patterns, and geochemical controls on gold mineralization remain poorly constrained. This study integrates petrographic analysis, X-ray diffraction (XRD), and X-ray fluorescence (XRF) geochemistry to characterize gold-bearing host rocks and evaluate the exploration significance of stream sediments. Thirteen rock samples and ten stream sediment samples were collected, from which ten representative rock specimens were analyzed by thin-section petrography and XRD, while ten host rocks and ten stream sediments were analyzed for major oxides and trace elements using XRF. Petrographic observations identified quartz, orthoclase, plagioclase, biotite, muscovite, chlorite, garnet, hornblende, and opaque minerals, with widespread sericitization, chloritization, silicification, and localized oxidation. XRD analysis confirmed quartz as the dominant mineral phase (39–69.2 wt.%), accompanied by orthoclase (6.0–30.4 wt.%), albite (0.2–21.0 wt.%), muscovite (0.1–34.0 wt.%), clinochlore (12.0–19.0 wt.%), goethite (0.06–6.2 wt.%), and minor anorthite (5.6–5.7 wt.%). Whole-rock geochemistry revealed SiO_2 contents ranging from 52.95 to 95.62 wt.% and K_2O contents from 0.15 to 10.88 wt.%, reflecting extensive silicification and sericitic alteration. Gold concentrations in host rocks varied from below detection to 126.24 ppm, with the highest values occurring in quartz veins and structurally controlled phyllite–gneiss contact zones. Stream sediment geochemistry identified pronounced gold anomalies of 216.12 ppm, 129.93 ppm, and 122.96 ppm at RSS2, RSS3, and RSS1, respectively, whereas northern drainage sediments contained only background concentrations (18.50–20.06 ppm) or no detectable gold. The integrated mineralogical and geochemical evidence indicates that gold mineralization is associated with hydrothermal fluids that migrated along NE–SW-trending shear zones and quartz veins during the Pan-African Orogeny, producing silicification, sericitization, chloritization, and subsequent supergene oxidation. The close spatial association between hydrothermal alteration, quartz veining, and elevated gold concentrations establishes reliable mineralogical and geochemical vectors for future exploration within the Mararaban Yauri area and comparable Precambrian orogenic gold systems of the Nigerian Basement Complex.*

Keywords: Gold mineralization, Hydrothermal alteration, Sericitisation, Chloritisation, Zuru Schist Belt, Stream sediment geochemistry.

Samaila Garba Riskuwa
Department of Geology and Mining, Nasarawa State University, Keffi, Nasarawa State, Nigeria
Email: samailariskuwa002@gmail.com
https://orcid.org/0009-0001-6581-4393

Ishak Yau Tanko
Department of Geology and Mining, Nasarawa State University, Keffi, Nigeria
Email: iyantanko@nsuk.edu.ng

1.0 Introduction

Also available @ doi.org/10.5281/zenodo.21292865

Gold mineralization in the Nigerian Basement Complex is principally hosted in quartz vein systems and shear zones developed within Precambrian metasedimentary and metavolcanic sequences that were extensively reworked during the Pan-African Orogeny (~600 Ma) (Garba, 2003; Okonkwo et al., 2021). Orogenic gold deposits constitute one of the world's most economically important sources of gold and are typically associated with structurally controlled hydrothermal systems developed during regional metamorphism and tectonic deformation. The mineralogy, alteration assemblages, and geochemical signatures preserved within host rocks provide valuable information on ore-forming processes and serve as reliable exploration guides in Precambrian terranes.

Orogenic gold deposits constitute one of the world's most economically important sources of gold and are typically associated with structurally controlled hydrothermal systems developed during regional metamorphism and tectonic deformation. The mineralogy, alteration assemblages, and geochemical signatures preserved within host rocks provide valuable information on ore-forming processes and serve as reliable exploration guides in Precambrian terranes.The mineralogical and geochemical characteristics of the host rocks and their hydrothermal alteration assemblages are fundamental to understanding ore genesis, constraining the physicochemical conditions of fluid–rock interaction, and defining geochemical vectors for exploration targets. The Nigerian Schist Belts are widely recognized as part of the global orogenic gold province, where hydrothermal alteration mineralogy and geochemical pathfinder element associations provide important criteria for distinguishing mineralized structures from barren lithologies and for identifying prospective exploration targets (Groves et al., 1998; Goldfarb et al., 2001).The Zuru Schist Belt of northwestern Nigeria is one of the most prospective gold-bearing terranes in the country. Despite a long history of artisanal mining at numerous localities, systematic mineralogical and geochemical characterization of the gold-bearing rocks remains limited in the Mararaban Yauri segment of the belt (Garba, 2000; Abdullahi et al., 2022). Previous investigations have focused principally on structural or regional geological frameworks, while detailed XRD mineralogy and XRF whole-rock geochemistry integrated with petrographic observation are largely absent for this area. Previous studies within the Zuru Schist Belt have primarily emphasized regional geological mapping, structural controls on mineralization, and reconnaissance exploration. However, few investigations have integrated petrographic observations with quantitative mineralogical and geochemical techniques to establish alteration paragenesis and mineralization pathways within the Mararaban Yauri area. Consequently, the mineralogical controls on gold precipitation, hydrothermal alteration zoning, fluid–rock interaction processes, and geochemical dispersion patterns remain inadequately constrained, thereby limiting the development of reliable exploration models for the area.To address these knowledge gaps, this study integrates petrographic analysis, X-ray diffraction (XRD), and X-ray fluorescence (XRF) techniques to provide a comprehensive mineralogical and geochemical characterization of gold-bearing rocks and stream sediments from the Mararaban Yauri area.The specific objectives of this study are to: (i) characterize the mineralogy, textures, and alteration features of the host rock lithologies through petrographic analysis; (ii) quantify the hydrothermal mineral assemblages using XRD and establish their paragenetic sequence; (iii) determine the major oxide and trace element geochemistry of host rocks and stream sediments using XRF; (iv) establish the spatial distribution of gold and pathfinder elements; and (v) integrate mineralogical and geochemical datasets to constrain the genesis

of the mineralizing system and define exploration vectors. This integrated analytical approach provides new insights into the mineralogical evolution of hydrothermal alteration, the geochemical characteristics of gold mineralization, and the exploration potential of the Mararaban Yauri segment of the Zuru Schist Belt. The integrated mineralogical and geochemical datasets generated in this study provide a scientific basis for understanding the genesis of gold mineralization and identifying exploration vectors within the Mararaban Yauri goldfield, Kebbi State, Nigeria.**1.1 Local Geological Setting**

The study area is situated in Mararaban Yauri, Ngaski Local Government Area, Kebbi State, northwestern Nigeria, within Yelwa Sheet 118 NE (longitudes 04°46′12″E–04°48′54″E; latitudes 10°44′51″N–10°46′08″N). The area covers approximately 20 km² and falls within the Zuru Schist Belt of the Precambrian Nigerian Basement Complex (Fig.1).

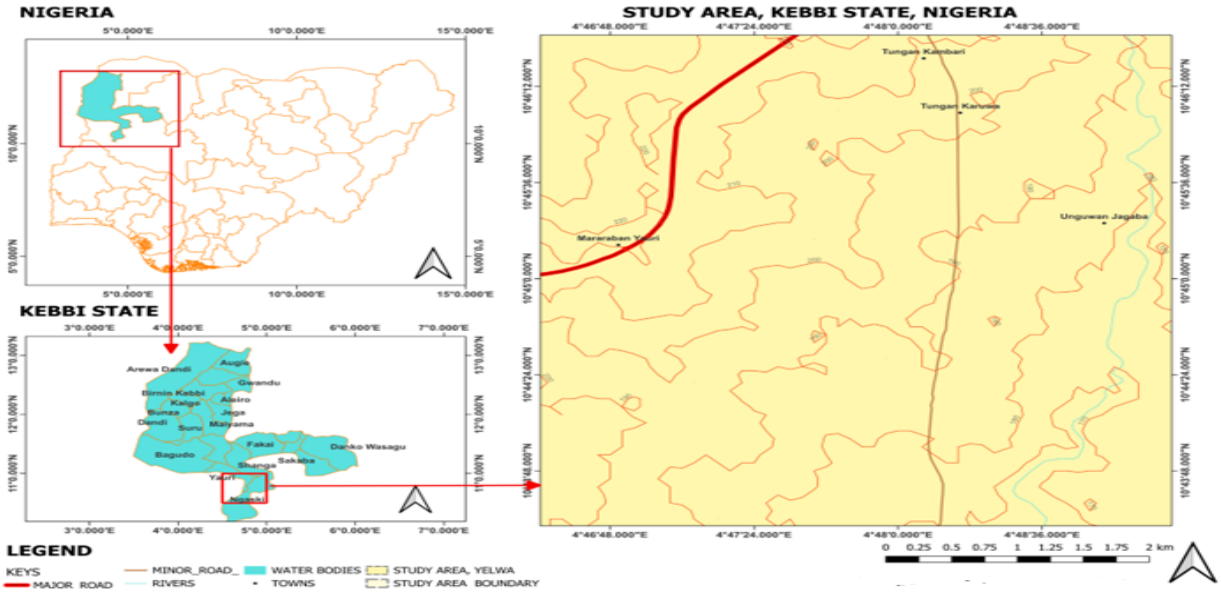

Fig. 1: Location and regional geological maps of the study area

The belt comprises of palaeoproterozoic (~2000 Ma) metasedimentary and metavolcanic sequences intruded by syn- to post-tectonic granitoids, extensively reworked during the Pan-African Orogeny (~600 Ma). The dominant Pan-African structural fabric is NE–SW, expressed through foliations, shear zones, fractures, and quartz vein systems that constitute the principal conduits for hydrothermal fluid migration and gold deposition in the belt. The study area lies within one of the major Pan-African metallogenic provinces of West Africa, where prolonged tectonic deformation, metamorphism, and hydrothermal fluid circulation have resulted in the emplacement of numerous auriferous quartz veins. These geological processes have created favourable structural traps for economically significant gold mineralization. Two major lithological units underlie the study area: phyllite (35–40 % of the mapped area), a low-grade metasedimentary rock occupying the central to south-central sector; and granitic gneiss (60–65%), a higher-grade metamorphic basement rock forming the dominant framework. Secondary quartz veins intrude both units along NE–SW fractures and shear zones are the principal gold-bearing structures targeted by artisanal miners. The geological map shows the distribution of these units and the ten host rock sampling stations (Fig. 2). Hydrothermal alteration associated with these

quartz veins is commonly manifested by sericitization, chloritization, silicification, and sulphide mineralization, which are important indicators of fluid evolution and ore deposition.

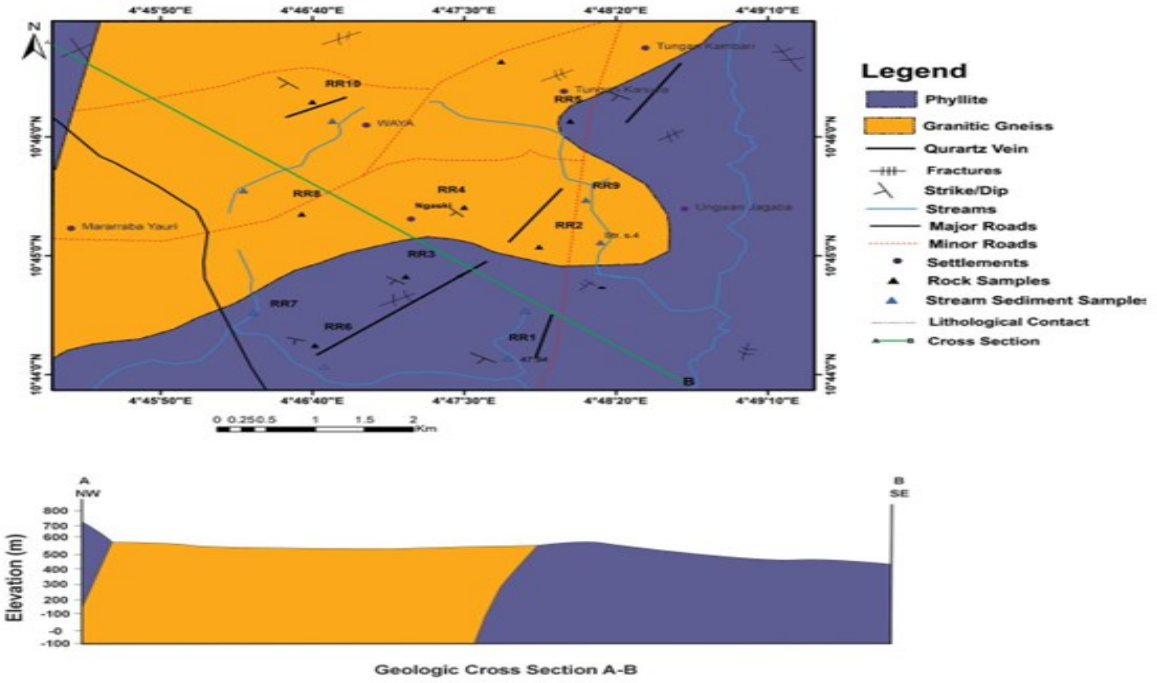

Fig. 2: Sampling Location Map of the Mararaban Yauri Study Area

3.0 Methodology

3.1 Sample Collection and Preparation

A total of thirteen representative rock samples were collected from quartz veins and their host rocks across ten sampling locations. From these, ten representative samples were selected for petrographic and XRD analyses based on their lithological characteristics and degree of mineralization. In addition, ten host-rock samples (RR1–RR10) and ten stream-sediment samples (RSS1–RSS10) were prepared for XRF geochemical analysis. Stream sediment samples were collected from active river channels beds at approximately 30 cm below the sediment surface contamination. All samples were weighed, coded, and divided into analytical portions before laboratory processing. Sample preparation for XRD involved pulverized using an agate mortar and pestle and sieved to obtain particles smaller than 63 μm and storage in labelled polyethene bags to prevent contamination and mix-up.

3.2 Thin-Section Petrography

Polished thin sections were prepared from ten representative rock specimens and examined under a Leica DM4P polarized microscope in both plane-polarized light (PPL) and crossed-polarized light (XPL) at a magnification of ×40. Mineral identification was based on optical properties such as colour, relief, cleavage, pleochroism, birefringence, interference colour, twinning, and extinction angle. Modal mineral proportions were determined using a 300-point count method for each thin section. Photomicrographs were acquired using a digital camera attached to the microscope for subsequent mineralogical interpretation.

3.3 X-Ray Diffraction (XRD) Analysis

XRD analysis was performed on ten powdered host rock samples at the National Steel Raw *Prior to analysis, powdered samples were homogenized and back-loaded into sample holders to minimize preferred orientation.* Materials and Exploration Agency (NSRMEA) laboratory, Kaduna. Samples were scanned

from 5° to 70° 2θ using CuKα radiation (λ = 1.5406 Å) at 40 kV and 40 mA. The scan step size was 0.02° 2θ with a counting time of 1 s per step. Diffractograms were matched against the ICDD PDF-4+ reference database for phase identification. Quantitative phase proportions were determined by Rietveld refinement using MAUD software. The quality of the refinement was evaluated using Rwp, Rp, and χ^2 goodness-of-fit statistics. Results were reported in weight percent (wt.%).

3.4 X-Ray Fluorescence (XRF) Geochemistry

Major oxide (SiO_2, Al_2O_3, Fe_2O_3, CaO, MgO, K_2O, TiO_2, MnO, P_2O_5, Na_2O, and SO_3 in wt.%) and trace element (including Au, As, Cu, Pb, Zn, Rb, Sr, Zr, Ba, Cr, Ni, Co, V, Ag, Sn, W, Nb, Cs, and Ta in ppm) concentrations were determined for the ten host rock samples and ten stream sediment samples using a wavelength-dispersive X-ray fluorescence (WD-XRF) spectrometer, Model: PANalytical Axios / Rigaku ZSX Primus / Bruker S8 Tiger (whichever instrument was actually used). . Instrument calibration was performed using certified international geological reference materials.Loss on ignition (LOI) was determined gravimetrically by ignition at 1000 °C for 1 hour. All major element totals were within 99.5–101.0 wt.%, indicating acceptable analytical quality. Gold concentrations were determined by fire assay followed by atomic absorption spectrometry (FAAS), with a detection limit of 0.5 ppb, whereas all other major and trace elements were determined by WD-XRF. Analytical precision and accuracy were assessed through repeated analyses of certified reference materials, procedural blanks, and duplicate samples. Detection limits for major oxides and trace elements followed the manufacturer's analytical specifications

4.0 Results and Discussion

4.1 Petrographic Observations

Petrographic examination of the ten representative rock samples identified two principal host lithologies, namely phyllite and granitic gneiss, together with mineralized quartz veins. The rocks are dominated by quartz, feldspars (orthoclase and plagioclase), biotite, muscovite, chlorite, garnet, hornblende, sericite, and minor opaque minerals. Textural observations reveal evidence of deformation, recrystallization, and hydrothermal alteration, including undulose extinction in quartz, sericitization, chloritization, and the development of opaque oxide minerals. Representative photomicrographs illustrating these petrographic characteristics are presented in Plates 1–10.

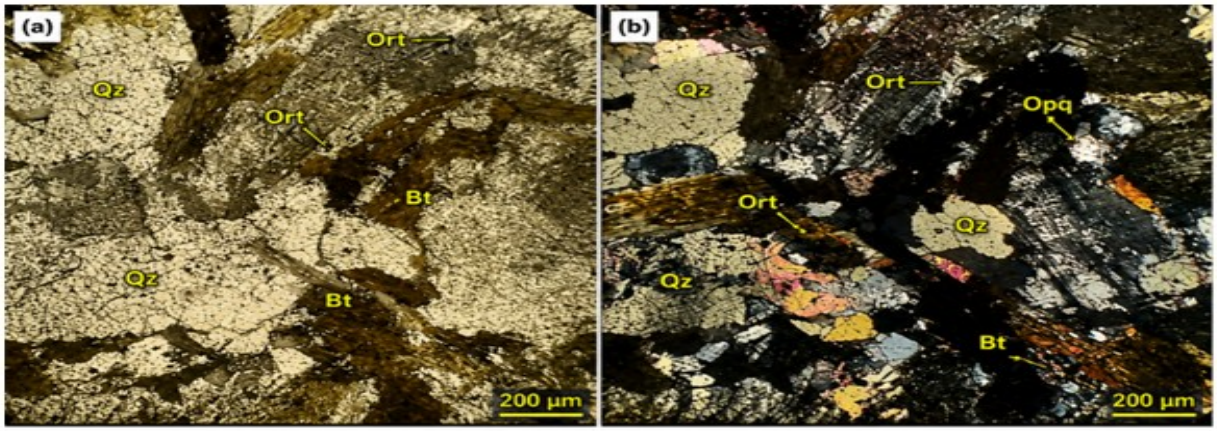

Plate 1: Photomicrograph of phyllite (RR1) under (a) Plane polarized light (PPL) and (b) Crossed polarized light (XPL), showing Qz = Quartz, Bt = Biotite, Ort = Orthoclase, and Opq = Opaque minerals; Mag. = X400

Under (a) Plane polarized light (PPL): Quartz occurs as colourless, anhedral to subhedral grains with undulose extinction. Biotite occurs as brown, pleochroic flakes with perfect basal cleavage and preferred orientation. Orthoclase appears as colourless to pale grains with perthitic texture. While (b) Crossed polarized light (XPL); Quartz shows low first-order grey to white interference colours. Biotite exhibits strong pleochroism with bright interference colours (orange, yellow, blue). Orthoclase displays tartan (cross-hatched) twinning. Opaque minerals appear black and are disseminated within the matrix.

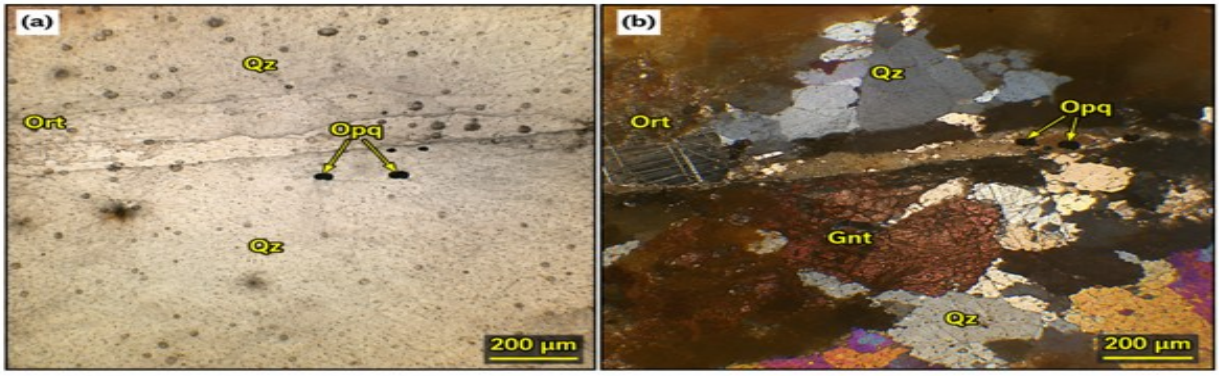

Plate 2: Photomicrograph of quartz vein (RR2): (a) Plane polarized light (PPL) and (b) Crossed polarized light (XPL), showing Qz = Quartz, Gnt = Garnet, Ort = Orthoclase, and Opq = (Fe-oxide/Fe-Ti oxide); Mag. = X400

Under (a) Plane polarized light (PPL): Quartz occurs as colourless, anhedral to subhedral grains with low relief. Orthoclase appears colourless with faint cleavage. Opaque minerals (Fe-oxide/Fe-Ti oxide) occur as fine disseminated to subrounded grains and as fillings along microfractures. Whereas Under (a) Crossed polarized light (XPL): Quartz shows low first-order grey to white interference colours with undulose extinction. Garnet appears in high relief with bright interference colours (pink, orange, yellow) and isotropic to weakly anisotropic character. Orthoclase displays tartan (cross-hatched) twinning. Opaque minerals remain black and occur along veinlets and grain boundaries.

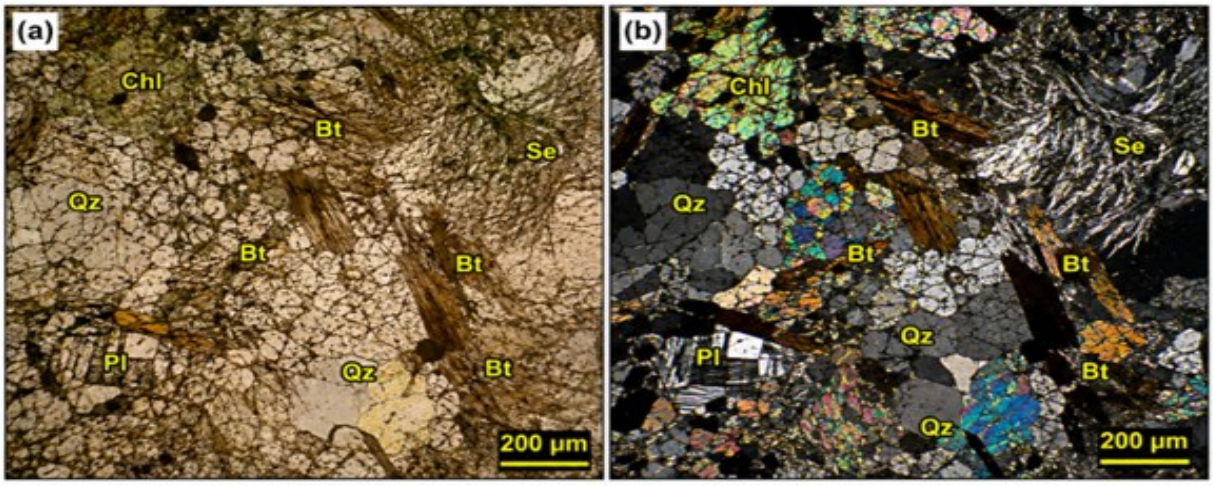

Plate 3: Photomicrograph of quartz vein (RR3): (a) Plane polarized light (PPL) and (b) Crossed polarized light (XPL), showing Qz = Quartz, Bt = Biotite, Pl = Plagioclase, Se = Sericite, and Chl = Chlorite, Mag. = X400

a) PPL: Quartz occurs as colourless, anhedral to subhedral grains with low relief. Biotite appears as brown, pleochroic flakes with perfect basal cleavage. Plagioclase is colourless with faint cleavage. Sericite forms fine, colourless to pale grey fibrous aggregates. Chlorite occurs as pale greenish, fine-grained patches partly replacing biotite and plagioclase.

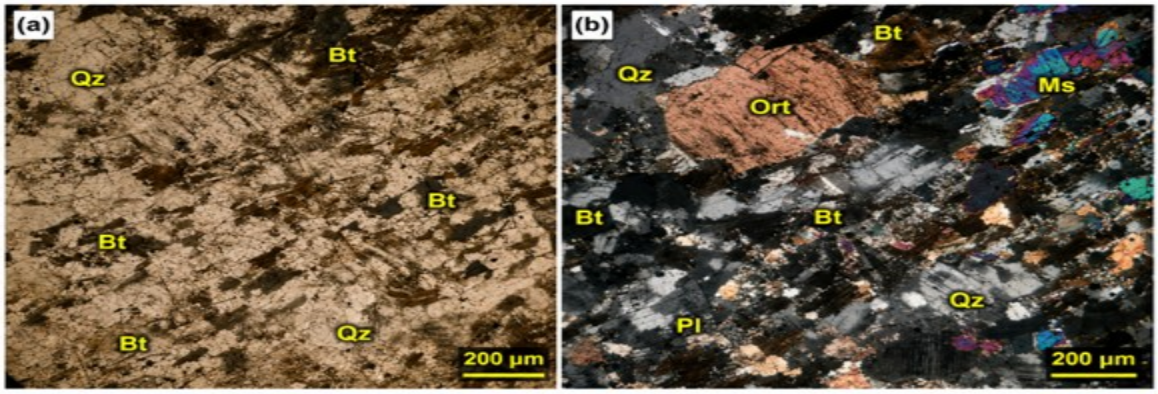

Plate 4: Photomicrograph of granitic gneiss (RR4): (a) Plane polarized light (PPL) and (b) Crossed polarized light (XPL), showing Qz = Quartz, Bt = Biotite, Pl = Plagioclase, Ort = Orthoclase, and Ms = Muscovite, Mag. = X400

(b) XPL: Quartz shows low first-order grey to white interference colours with undulose extinction. Biotite exhibits strong pleochroism with bright interference colours (orange, yellow, brown). Plagioclase displays polysynthetic (albite) twinning. Sericite remains low birefringent (grey-white). Chlorite shows anomalous blue-green interference colours.

(a) PPL: Quartz occurs as colourless, anhedral to subhedral grains with low relief. Biotite appears as brown, pleochroic flakes with perfect basal cleavage. Plagioclase is colourless with faint cleavage and polysynthetic striations. Orthoclase is colourless to pale pink with distinct cleavage. Muscovite occurs as colourless, flaky plates with good basal cleavage.

(b) XPL: Quartz shows low first-order grey to white interference colours. Biotite exhibits strong pleochroism with bright interference colours (orange, yellow, brown). Plagioclase displays polysynthetic (albite) twinning. Orthoclase shows tartan (cross-hatched) twinning. Muscovite displays high birefringence with bright interference colours (blue, green, pink).

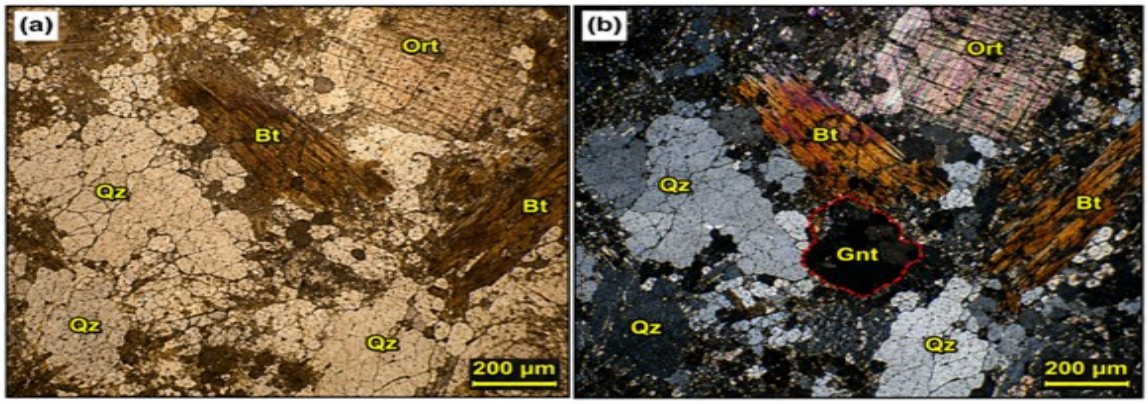

Plate 5: Photomicrograph of quartz vein (RR5)under (a) Plane polarized light (PPL) and (b) Crossed polarized light (XPL) showing Qz=Quartz, Bt=Biotite, Ort=Orthoclase, and Gnt=Garnet, Mag. =X400

(

a) PPL: Quartz occurs as colourless, anhedral grains with low relief and undulose extinction. Biotite appears as brown, pleochroic flakes with perfect basal cleavage. Orthoclase is colourless to pale pink with distinct cleavage and perthitic texture. Garnet is not readily distinguished under PPL but occurs as subhedral grains.

(b) XPL: Quartz shows low first-order grey to white interference colours. Biotite exhibits moderate to high birefringence with bright interference colours (orange, yellow, brown). Orthoclase displays tartan (cross-hatched) twinning and low-order interference colours. Garnet occurs as isotropic grains (black) due to high relief and is clearly outlined.

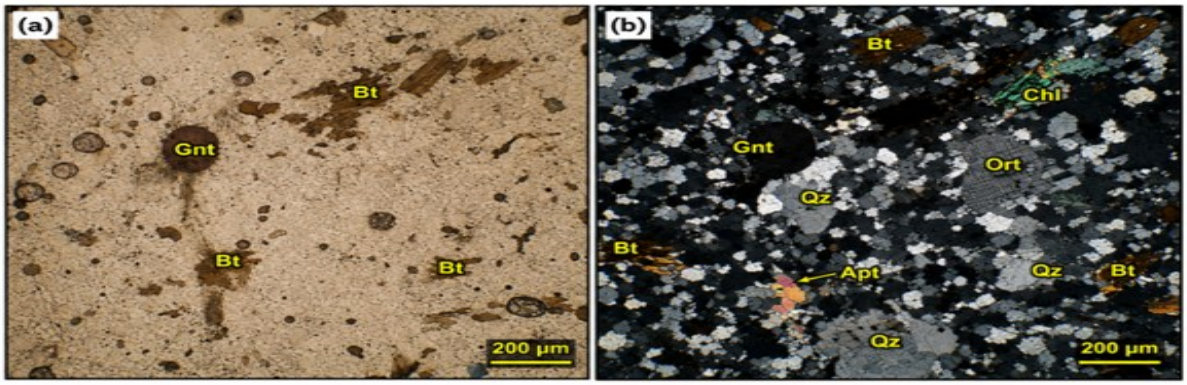

Plate 6: Photomicrograph of phyllite (RR6): (a) Plane polarized light (PPL) and (b) Crossed polarized light (XPL), showing Qz = Quartz, Bt = Biotite, Gnt = Garnet, Ort = Orthoclase, and Chl = Chlorite, Mag. = X400

(a) PPL: Quartz occurs as colourless, anhedral grains with low relief. Biotite appears as brown, pleochroic flakes with perfect basal cleavage. Garnet occurs as subhedral to anhedral grains with high relief and is often brownish. Orthoclase is colourless with distinct cleavage. Accessory apatite is not readily distinguished under PPL.

(b) XPL: Quartz shows low first-order grey to white interference colours. Biotite exhibits strong pleochroism with bright interference colours (orange, yellow, brown). Garnet is isotropic (black) due to high relief. Orthoclase displays tartan (cross-hatched) twinning. Chlorite shows anomalous green interference colours. Apatite occurs as small, high-birefringence grains with bright colours.

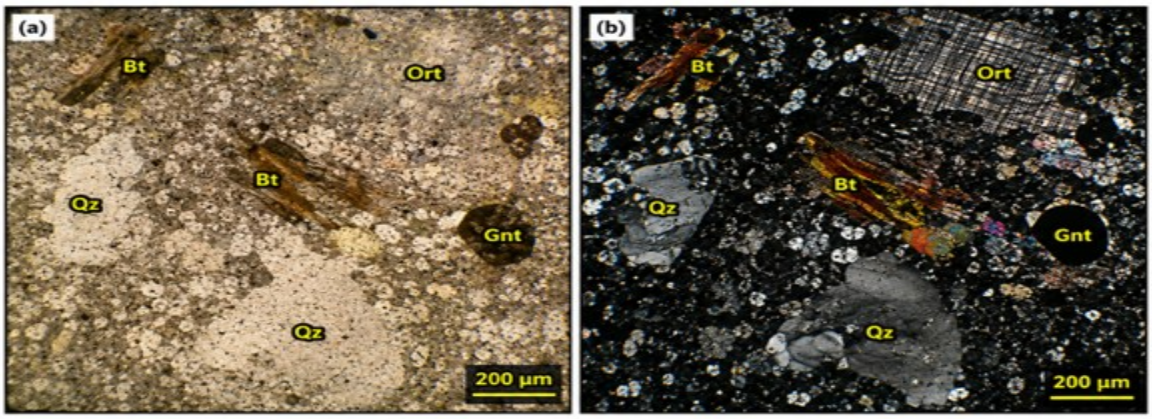

Plate 7: Photomicrograph of quartz vein (RR7): (a) Plane polarized light (PPL) and (b) Crossed polarized light (XPL), showing Qz = Quartz, Bt = Biotite, Ort = Orthoclase, and Gnt = Garnet, Mag. = X400

(a) PPL: Quartz occurs as colourless, anhedral grains with low relief. Biotite appears as brown, pleochroic flakes with perfect basal cleavage. Orthoclase is colourless to pale pink with distinct cleavage and locally perthitic texture. Garnet occurs as subhedral grains and appears brownish due to high relief.

(b) XPL: Quartz shows low first-order grey to white interference colours with undulose extinction. Biotite exhibits strong pleochroism with bright interference colours (orange, yellow, brown). Orthoclase displays tartan (cross-hatched) twinning and low-order interference colours. Garnet occurs as isotropic grains (black) due to high relief.

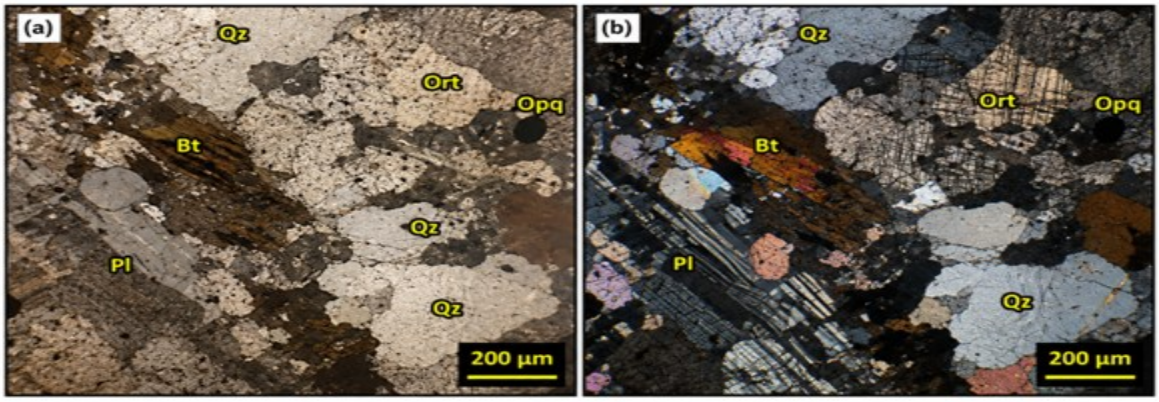

Plate 8: Photomicrograph of granitic gneiss (RR8): (a) Plane polarized light (PPL) and (b) Crossed polarized light (XPL), showing Qz = Quartz, Bt = Biotite, Pl = Plagioclase, Ort = Orthoclase, and Opq = (Fe-oxide/Fe-Ti oxide), Mag. = X400

(a) PPL: Quartz occurs as colourless, anhedral grains with low relief. Biotite appears as brown, pleochroic flakes with perfect basal cleavage. Plagioclase is colourless to grey with obvious cleavage. Orthoclase is colourless to pale pink with indistinct cleavage and locally perthitic texture. Opaque minerals occur as black, non-transmitting grains.

(b) XPL: Quartz shows low first-order grey to white interference colours with undulose extinction. Biotite exhibits strong pleochroism with bright interference colours (orange-yellow-brown). Plagioclase shows polysynthetic (albite) twinning with low-order interference colours. Orthoclase displays tartan

(cross-hatched) twinning. Opaque minerals remain black under crossed polars.

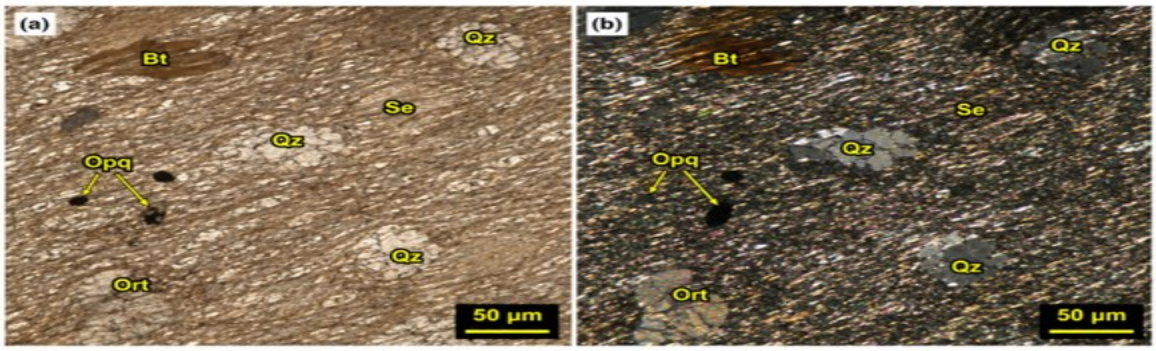

Plate 9: Photomicrograph of phyllite (RR9): (a) Plane polarized light (PPL) and (b) Crossed polarized light (XPL), showing Qz. = Quartz, Bt. =Biotite, Se. =Sericite, Ort. = Orthoclase, and Opq. = (Fe-oxide/Fe-Ti oxide); Mag. = X400

(a) PPL: Quartz occurs as colourless, fine-grained aggregates with low relief and undulose extinction. Biotite appears as brown, pleochroic flakes with perfect basal cleavage. Sericite occurs as fine, colourless micaceous flakes with a silky sheen, defining the foliation. Orthoclase is colourless with low relief and indistinct cleavage. Opaque minerals occur as black, non-transmitting grains.

(b) XPL: Quartz shows low first-order grey to white interference colours with undulose extinction. Sericite exhibits low birefringence with faint interference colours due to its very fine grain size. Biotite displays strong pleochroism with bright interference colours (orange-yellow-brown). Orthoclase shows low-order interference colours with weak twinning. Opaque minerals remain black under crossed polars.

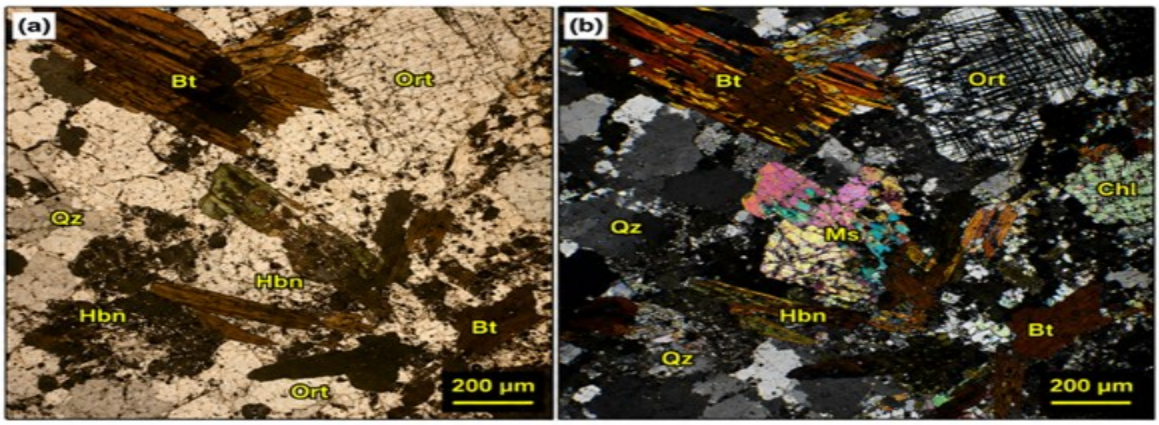

Plate 10: Photomicrograph of granitic gneiss (RR10): (a) Plane polarized light (PPL) and (b) Crossed polarized light (XPL), showing Qz. = Quartz, Bt. = Biotite, Hbn. = Hornblende, Ort. = Orthoclase, and Ms. = Muscovite, Mag. =*X400*

(a) PPL: Quartz occurs as colourless, anhedral grains with low relief. Biotite appears as brown, pleochroic flakes with perfect basal cleavage. Hornblende occurs as greenish-brown prismatic crystals with two cleavages at ~56°/124°. Orthoclase is colourless to pale pink with distinct cleavage and locally perthitic texture. Muscovite is present as colourless, flaky plates. Chlorite occurs as pale green alteration along grain margins.

(b) XPL: Quartz shows low first-order grey to white interference colours with undulose

extinction. Biotite exhibits strong pleochroism with bright interference colours (orange to yellow). Hornblende shows moderate birefringence (green-brown). Orthoclase displays tartan (cross-hatched) twinning. Muscovite shows high birefringence with bright pastel colours. Chlorite shows anomalous green interference colours.

Across all thin sections, quartz occurs predominantly as anhedral to subhedral grains displaying undulose extinction, indicating deformation associated with regional metamorphism. Orthoclase commonly exhibits tartan twinning, whereas plagioclase is characterized by polysynthetic twinning. Biotite occurs as pleochroic flakes aligned along foliation planes, while chlorite and sericite commonly replace biotite and feldspar, indicating hydrothermal alteration. Garnet is observed mainly within quartz veins and phyllitic rocks as subhedral to anhedral porphyroblasts, whereas hornblende is restricted to granitic gneiss. Disseminated opaque minerals frequently occupy fractures, grain boundaries, and alteration zones, suggesting late-stage mineralization.

4.2 Geochemistry

This section presents the mineralogical composition determined by X-ray diffraction (XRD) together with the major oxide and trace-element geochemistry obtained from X-ray fluorescence (XRF) analyses. The integrated datasets provide the mineralogical and geochemical characteristics of the host rocks and stream sediments within the Mararaban Yauri goldfield.

3.2.1 X-Ray Diffraction (XRD) Analysis

XRD analysis identified quartz, orthoclase, albite, muscovite, clinochlore, goethite, and anorthite as the mineral phases present across the ten host-rock samples (Tables 1–10). Quartz is the dominant phase in every sample; orthoclase and albite represent the feldspar group; muscovite and clinochlore occur as the principal secondary sheet silicates recording sericitic and chloritic alteration, respectively; goethite records supergene oxidation; and anorthite occurs locally as a calcium-rich plagioclase component.

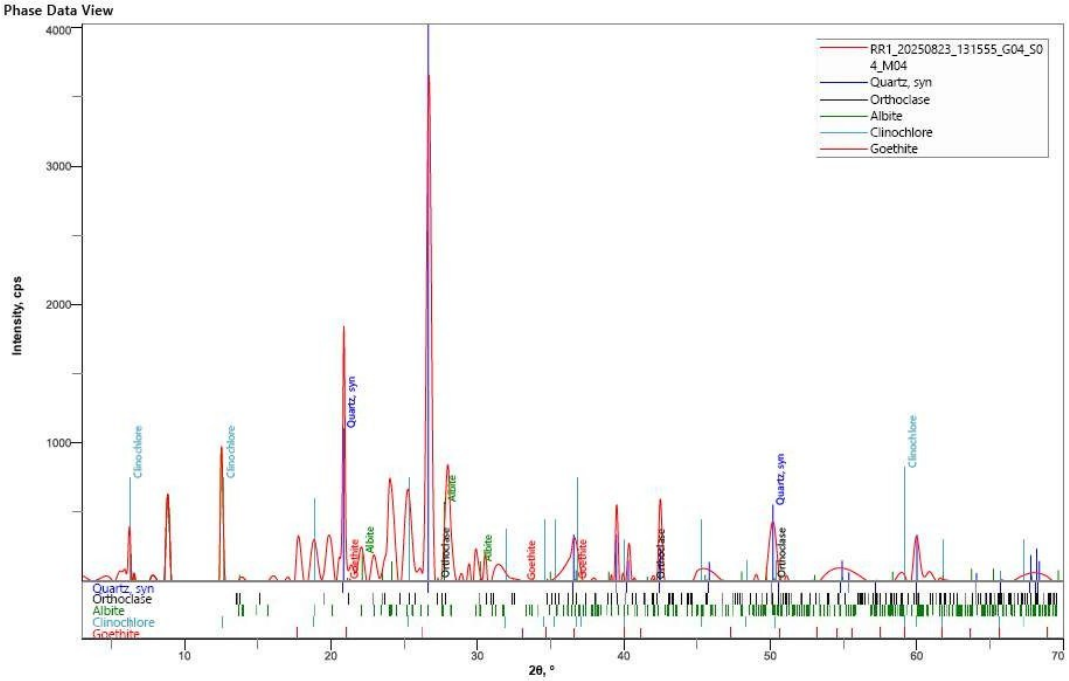

Fig.3: XRD diffractogram of Sample RR1 obtained using Cu-Kα radiation over a 2θ range of 5–70°, with phase identification by Rietveld refinement.

Table 1: Relative Abundance of Mineral Phases Identified by XRD Analysis (RR1)

Mineral Phase	Chemical Formula	RR1 (wt.%)
Quartz	SiO_2	54
Orthoclase	$KAlSi_3O_8$	14
Albite	$NaAlSi_3O_8$	10.3
Clinochlore	$(Mg,Fe)_5Al(Si_3Al)O_{10}(OH)_8$	19
Goethite	FeO(OH)	3.4

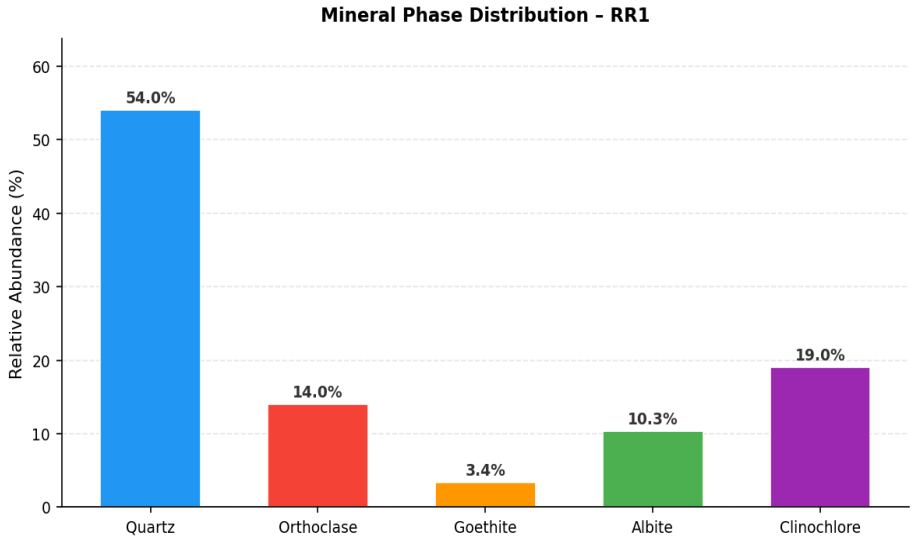

Fig. 4: Bar chart of relative mineral-phase abundance (%) for Sample RR1.

Quartz (54 wt.%) is the dominant phase, with clinochlore (19 wt.%) constituting a mineralogically significant secondary component that records chloritisation of the original biotite. Feldspar (orthoclase + albite, ~24 wt.%) remains largely preserved, indicating that sericitic replacement was subordinate to chloritic alteration at this locality. The minor goethite (3.4 wt.%) reflects incipient supergene oxidation of disseminated sulphides. This assemblage places RR1 within the propylitic-to-transitional zone of the hydrothermal system, consistent with its peripheral position relative to the sericite-dominated ore core, while its moderate gold content (47.94 ppm) confirms that the chloritic margin retains economically relevant mineralization.

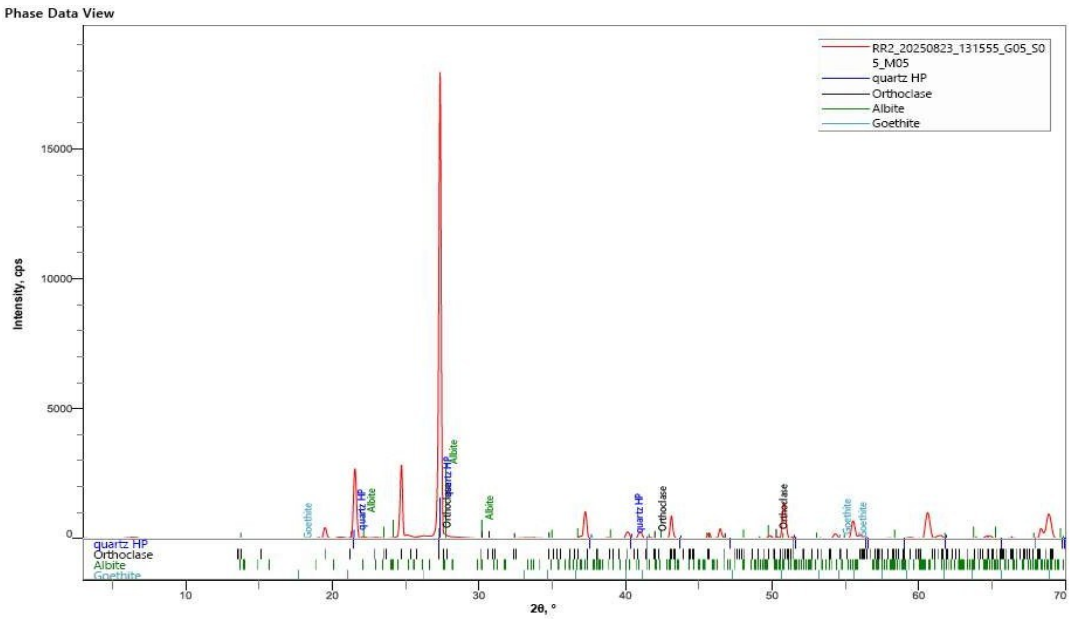

Fig. 5: XRD diffractogram of Sample RR2 obtained using Cu-Kα radiation over a 2θ range of 5–70°, with phase identification by Rietveld refinement.

Table 2: Relative Abundance of Mineral Phases Identified by XRD Analysis (RR2)

Mineral Phase	Chemical Formula	RR2 (wt.%)
Quartz	SiO_2	64
Orthoclase	$KAlSi_3O_8$	20
Albite	$NaAlSi_3O_8$	16
Goethite	FeO(OH)	0.2

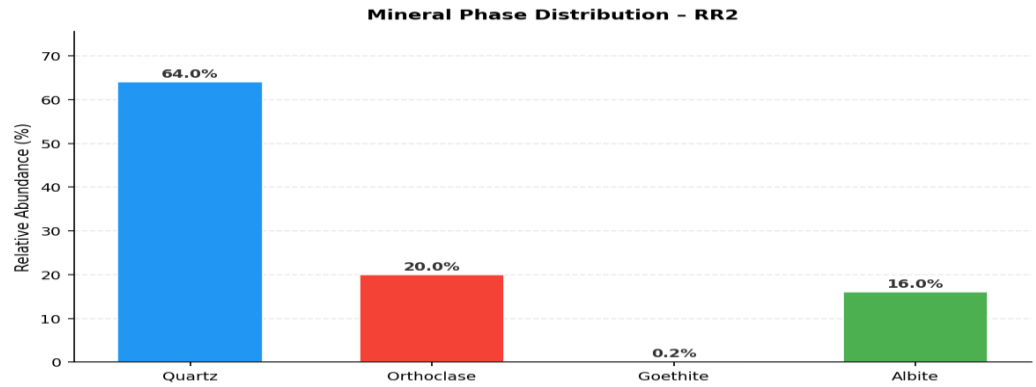

Fig, 6: Bar chart of relative mineral-phase abundance (%) for Sample RR2

The assemblage is dominated by quartz and primary feldspar (orthoclase + albite, 36 wt.%), with only trace goethite (0.2 wt.%) and a complete absence of sericite or chlorite. This near-unaltered mineralogy indicates that RR2 represents a structurally isolated, weakly reacted vein segment that was largely bypassed by the mineralizing hydrothermal fluid. The lack of alteration minerals correlates directly with the absence of detectable gold in this sample, reinforcing sericitisation and chloritisation as first-order mineralogical vectors to ore in this system rather than quartz vein occurrence alone.

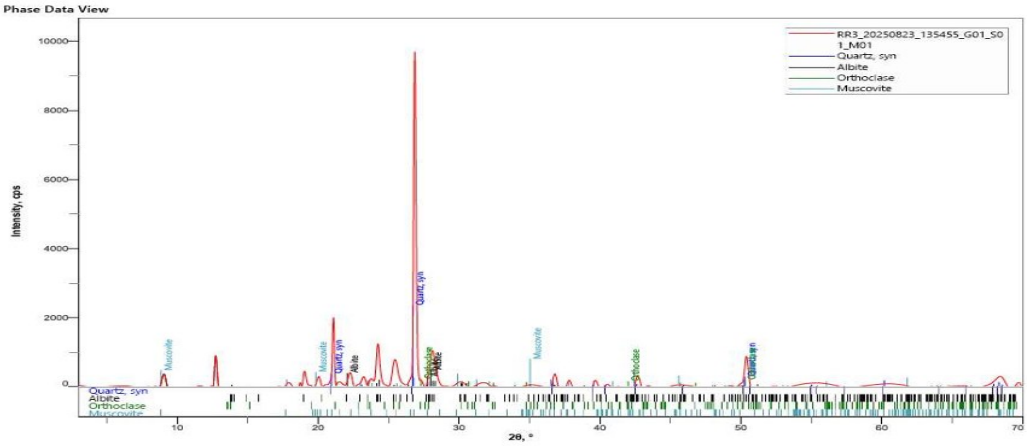

Fig. 7: XRD diffractogram of Sample RR3 obtained using Cu-Kα radiation over a 2θ range of 5–70°, with phase identification by Rietveld refinement.

Table 3: Relative Abundance of Mineral Phases Identified by XRD Analysis (RR3)

Mineral Phase	Chemical Formula	RR3 (wt.%)
Quartz	SiO_2	63
Orthoclase	$KAlSi_3O_8$	10.7
Albite	$NaAlSi_3O_8$	19.3
Muscovite	$H_2KAl_3(SiO_4)_3$	7

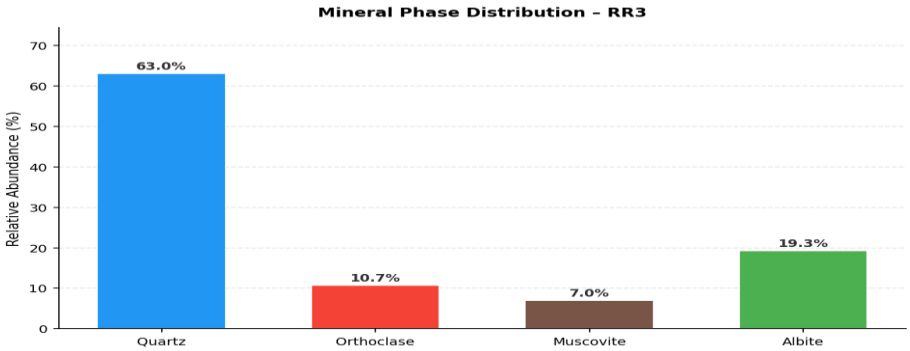

Fig. 8: Bar chart of relative mineral-phase abundance (%) for Sample RR3.

Quartz dominates the assemblage (63 wt.%), and the presence of muscovite (7 wt.%) confirms a sericitic overprint despite the absence of chlorite or goethite. This sample records the highest gold concentration in the host-rock suite (126.24 ppm), and its

coincidence with sericite rather than chlorite or supergene phases directly supports sericitisation as the principal mineralogical vector toward ore-grade gold. The absence of goethite suggests that primary sulphides at this structural level have not been substantially oxidised, consistent with RR3 representing a comparatively fresh, high-grade segment of the vein system.

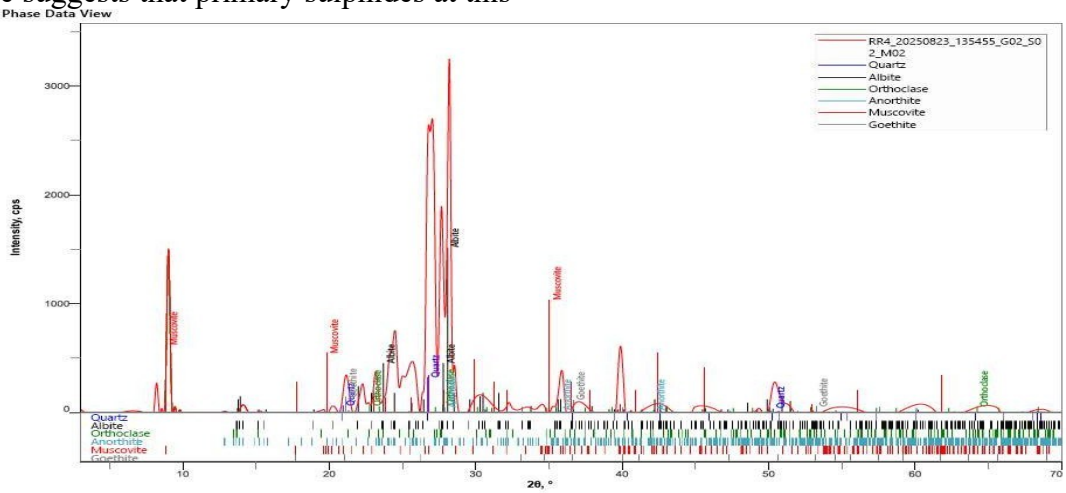

Fig. 9: XRD diffractogram of Sample RR4 obtained using Cu-Kα radiation over a 2θ range of 5–70°, with phase identification by Rietveld refinement.

Table 4: Relative Abundance of Mineral Phases Identified by XRD Analysis (RR4)

Mineral Phase	Chemical Formula	RR4 (wt.%)
Quartz	SiO_2	52
Orthoclase	$KAlSi_3O_8$	16
Albite	$NaAlSi_3O_8$	20
Muscovite	$H_2KAl_3(SiO_4)_3$	3.2
Goethite	$FeO(OH)$	4.1
Anorthite	$CaAl_2Si_2O_8$	5.7

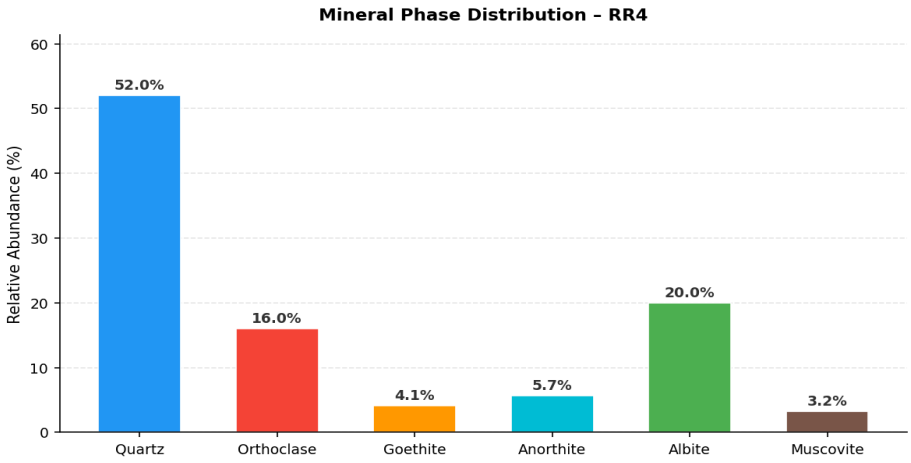

Fig. 10: Bar chart of relative mineral-phase abundance (%) for Sample RR4.

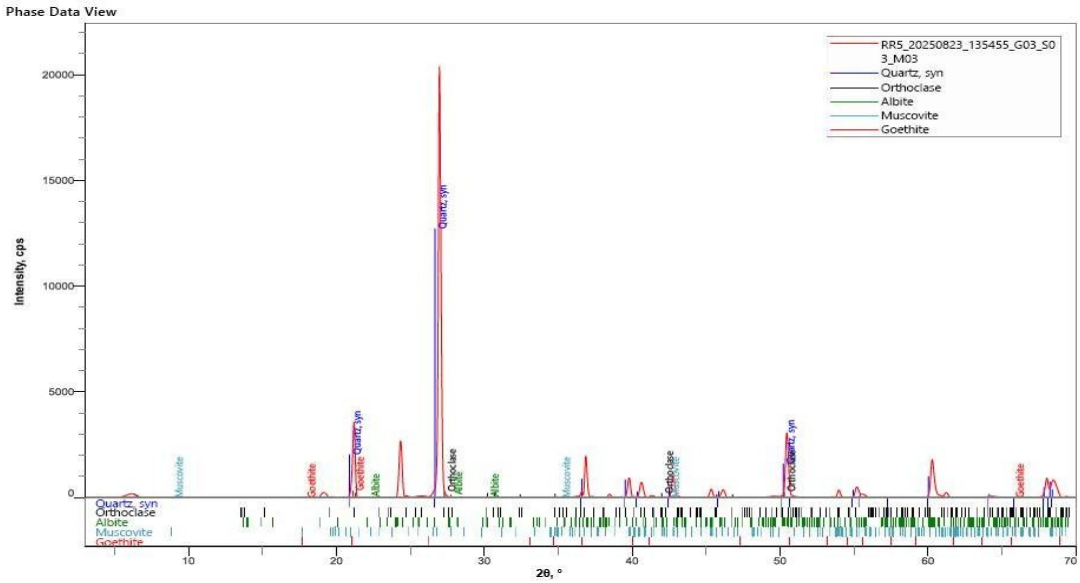

Fig. 11: XRD diffractogram of Sample RR5 obtained using Cu-Kα radiation over a 2θ range of 5–70°, with phase identification by Rietveld refinement.

RR4 retains a strongly feldspathic character (orthoclase + albite + anorthite ≈ 41.7 wt.%) reflecting its granitic gneiss protolith, with only weak sericitisation (3.2 wt.% muscovite). The moderate goethite content (4.1 wt.%) indicates measurable supergene oxidation of sulphides, coincident with the highest arsenic value recorded in the host-rock suite (23 ppm), consistent with an arsenopyrite precursor. The decoupling of appreciable goethite/arsenic from very low gold (3.35 ppm) suggests that sulphide oxidation at this site was not accompanied by significant primary gold deposition, marking RR4 as a distal, weakly mineralized facies of the hydrothermal system.

Table 5: Relative Abundance of Mineral Phases Identified by XRD Analysis (RR5)

Mineral Phase	Chemical Formula	RR5 (wt.%)
Quartz	SiO_2	69.2
Orthoclase	$KAlSi_3O_8$	30.4
Albite	$NaAlSi_3O_8$	0.2
Muscovite	$H_2KAl_3(SiO_4)_3$	0.1
Goethite	FeO(OH)	0.06

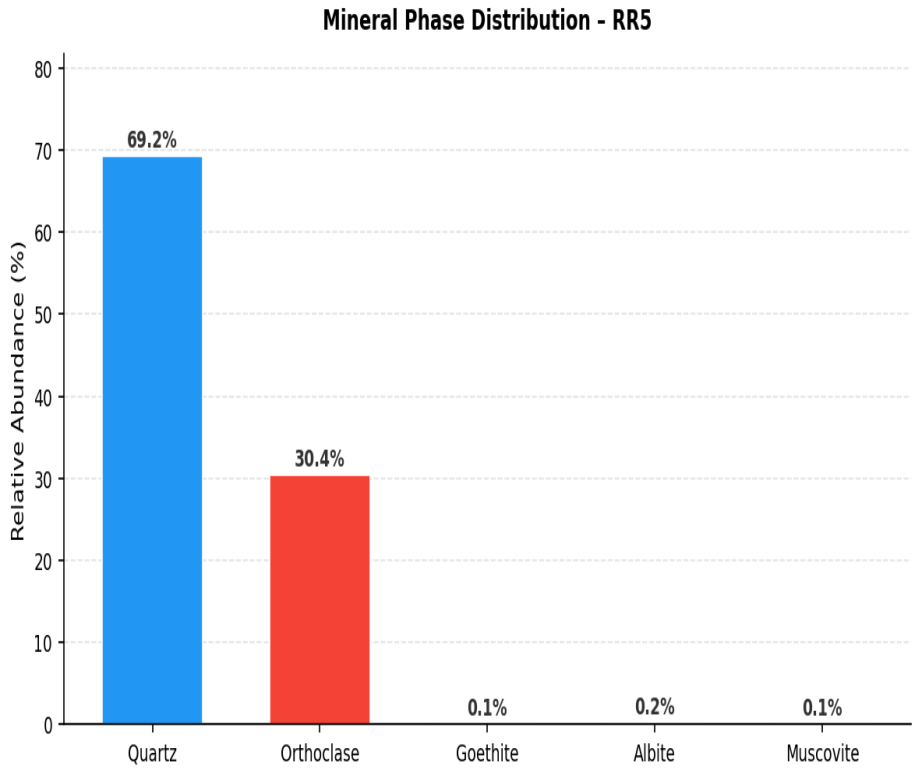

Figure 12: Bar chart of relative mineral-phase abundance (%) for Sample RR5.

Quartz and orthoclase together account for essentially the entire mineral budget (99.6 wt.%), with sericite, chlorite, and goethite all negligible. RR5 hosts the second-highest gold value in the suite (92.73 ppm), indicating that gold here is concentrated largely within a silica-feldspar vein matrix rather than an associated phyllosilicate alteration halo. Note that the reported orthoclase abundance (30.4 wt.%) is difficult to reconcile with the very low whole-rock K_2O content of this sample (0.15 wt.%; Table 11); this discrepancy could not be resolved from the data provided and should be re-examined against the raw diffractogram before submission.

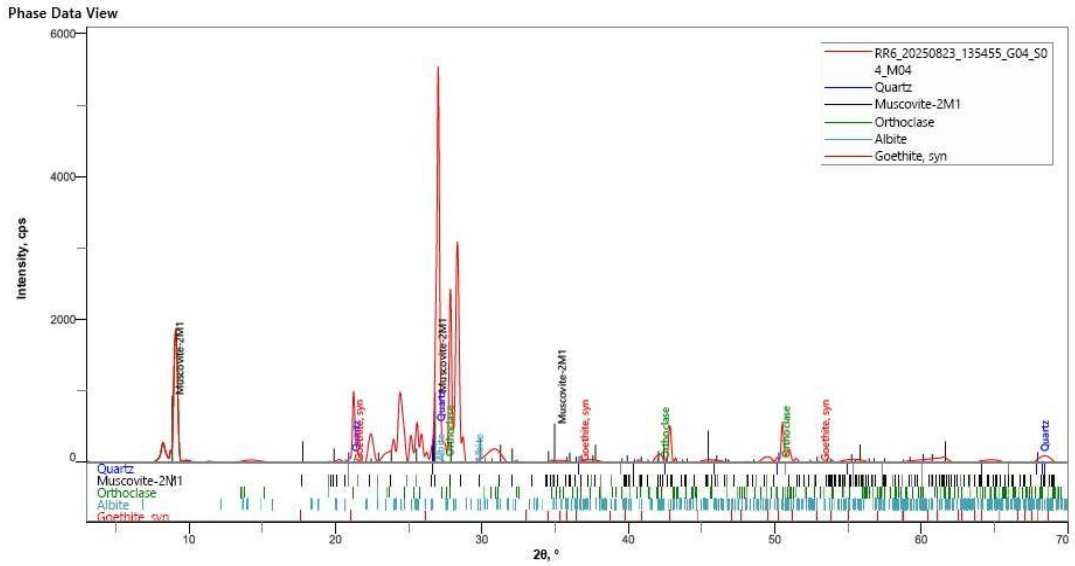

Fig.13: XRD diffractogram of Sample RR6 obtained using Cu-Kα radiation over a 2θ range of 5–70°, with phase identification by Rietveld refinement

Table 6: Relative Abundance of Mineral Phases Identified by XRD Analysis (RR6)

Mineral Phase	**Chemical Formula**	**RR6 (wt.%)**
Quartz	SiO_2	39
Orthoclase	$KAlSi_3O_8$	25.1
Albite	$NaAlSi_3O_8$	1.4
Muscovite	$H_2KAl_3(SiO_4)_3$	34
Goethite	FeO(OH)	0.4

Muscovite (34 wt.%) is co-dominant with quartz (39 wt.%), making RR6 the most intensely sericitised sample in the suite. This mineralogy coincides with the highest whole-rock K_2O (10.88 wt.%; Table 11) and with substantial gold (60.39 ppm), copper, and lead contents, identifying RR6 as representative of the inner potassic-to-sericitic alteration core of the hydrothermal system. The near-total depletion of albite (1.4 wt.%) and negligible goethite indicate advanced plagioclase destruction with minimal supergene overprint, consistent with a hypogene-dominated alteration signature at this locality.

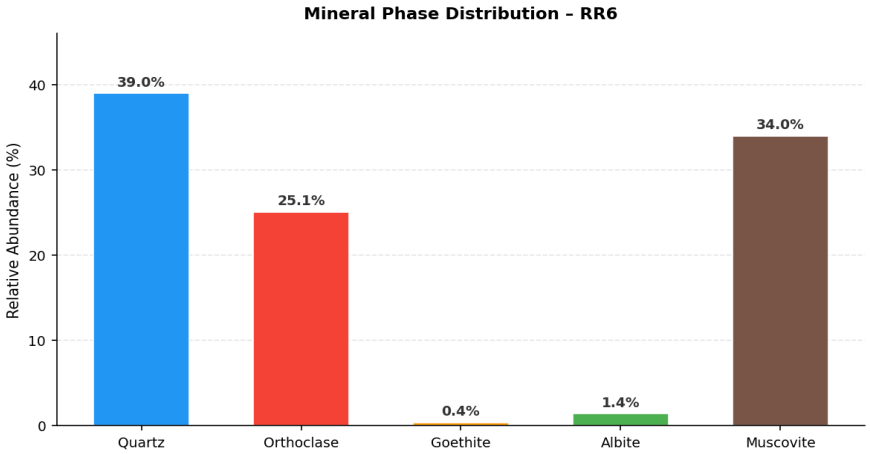

Fig. 14: Bar chart of relative mineral-phase abundance (%) for Sample RR6

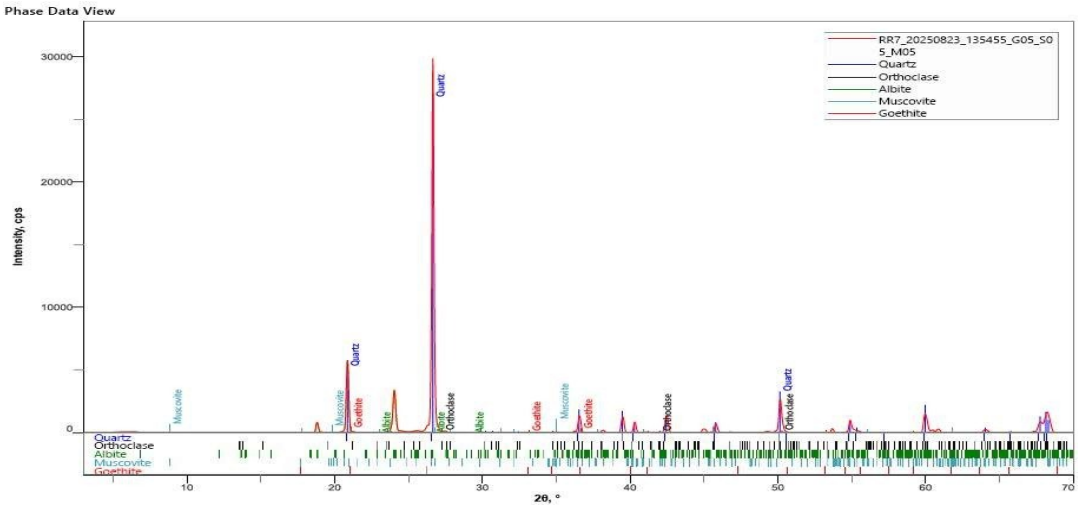

Fig. 15: XRD diffractogram of Sample RR7 obtained using Cu-Kα radiation over a 2θ range of 5–70°, with phase identification by Rietveld refinement

Table 7: Relative Abundance of Mineral Phases Identified by XRD Analysis (RR7)

Mineral Phase	Chemical Formula	RR7 (wt.%)
Quartz	SiO_2	68
Orthoclase	$KAlSi_3O_8$	24.3
Albite	$NaAlSi_3O_8$	5
Muscovite	$H_2KAl_3(SiO_4)_3$	2
Goethite	FeO(OH)	1

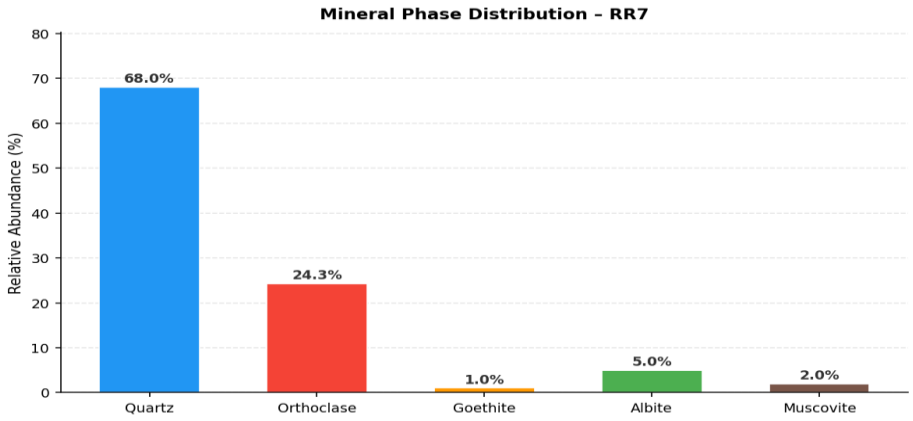

Fig. 16: Bar chart of relative mineral-phase abundance (%) for Sample RR7.

Quartz and orthoclase dominate (92.3 wt.% combined), with only minor sericite (2 wt.% muscovite) and weak goethite (1 wt.%) indicating a subdued alteration overprint. The moderate gold content (21.85 ppm), despite limited hydrothermal mineral development, suggests that gold in this sample resides largely within the quartz-vein matrix itself rather than being controlled by sericite abundance. RR7 is interpreted as a transitional vein facies between the strongly altered, ore-grade segments (e.g., RR3) and weakly reacted, near-barren vein material (e.g., RR2).

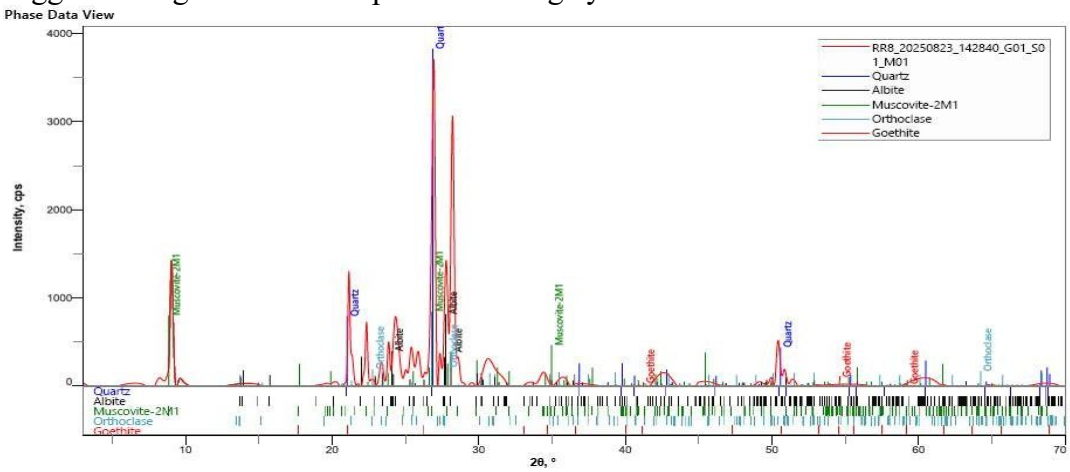

Figure 17: XRD diffractogram of Sample RR8 obtained using Cu-Kα radiation over a 2θ range of 5–70°, with phase identification by Rietveld refinement.

Table 8: Relative Abundance of Mineral Phases Identified by XRD Analysis (RR8)

Mineral Phase	**Chemical Formula**	**RR8 (wt.%)**
Quartz	SiO_2	40
Orthoclase	$KAlSi_3O_8$	17
Albite	$NaAlSi_3O_8$	21
Muscovite	$H_2KAl_3(SiO_4)_3$	23
Goethite	FeO(OH)	0.2

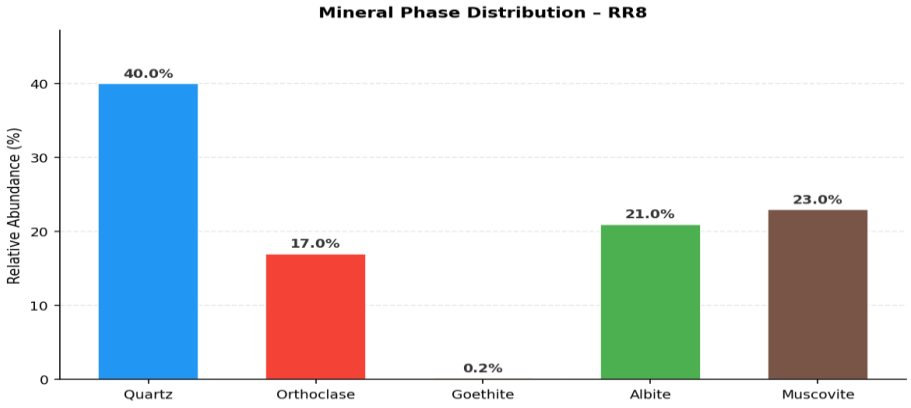

Fig. 18: Bar chart of relative mineral-phase abundance (%) for Sample RR8.

Muscovite (23 wt.%) is the second-highest sericite content in the dataset, indicating a strong sericitic overprint within the granitic gneiss host, alongside co-dominant quartz and albite. This mineralogy correlates with an elevated whole-rock K_2O (8.48 wt.%; Table 11) and moderate gold (32.34 ppm), and negligible goethite (0.2 wt.%) indicates minimal supergene modification. RR8 is therefore assigned to the inner sericitic alteration zone together with RR6, demonstrating that the sericitic core cross-cuts both principal host lithologies rather than being confined to phyllite alone.

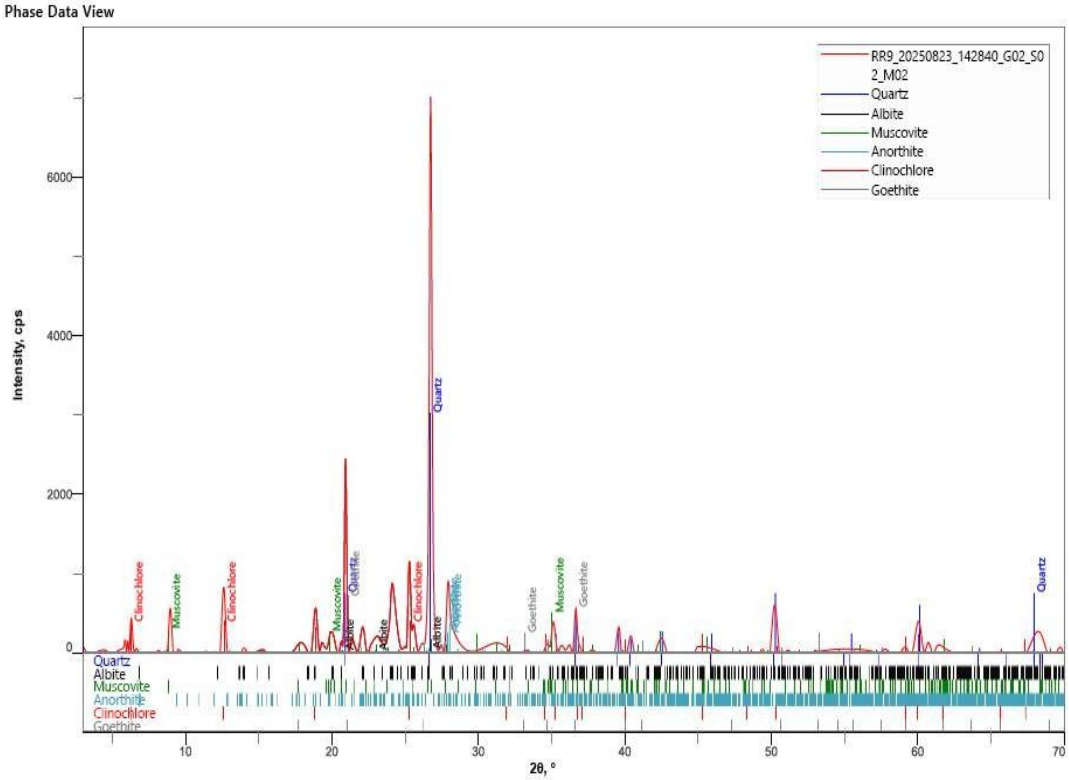

Fig. 19: XRD diffractogram of Sample RR9 obtained using Cu-Kα radiation over a 2θ range of 5–70°, with phase identification by Rietveld refinement

Table 9: Relative Abundance of Mineral Phases Identified by XRD Analysis (RR9)

Mineral Phase	Chemical Formula	RR9 (wt.%)
Quartz	SiO_2	62
Orthoclase	$KAlSi_3O_8$	6
Albite	$NaAlSi_3O_8$	6
Muscovite	$H_2KAl_3(SiO_4)_3$	8
Clinochlore	$(Mg,Fe)_5Al(Si_3Al)O_{10}(OH)_8$	12
Goethite	$FeO(OH)$	6.2
Anorthite	$CaAl_2Si_2O_8$	5.6

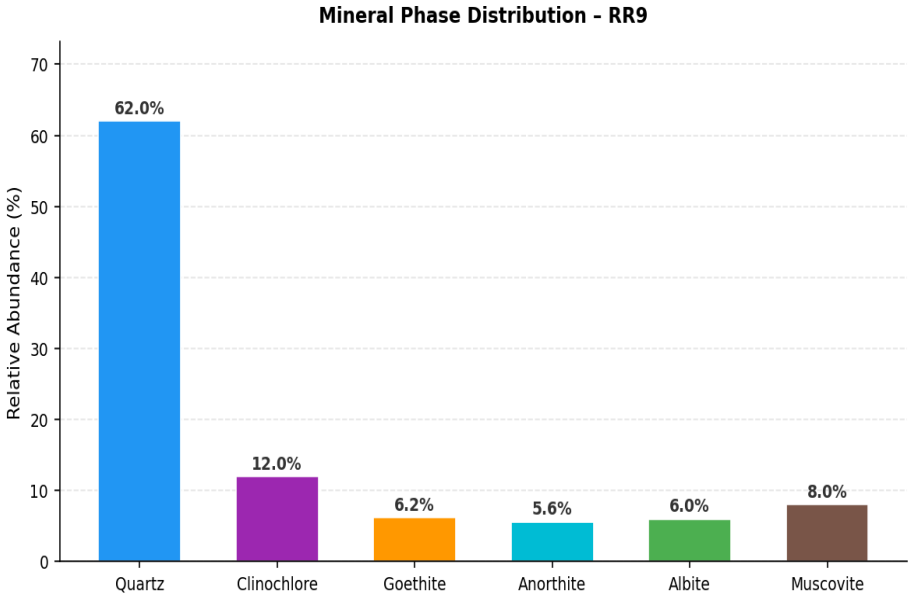

Fig.20: Bar chart of relative mineral-phase abundance (%) for Sample RR9.

RR9 hosts the most mineralogically complex assemblage in the suite, combining chlorite (12 wt.% clinochlore), moderate sericite (8 wt.% muscovite), and the highest goethite content recorded (6.2 wt.%). This combination records superposition of propylitic chloritisation and pervasive supergene oxidation on an originally sericitised protolith, making RR9 the single sample that best preserves the full hypogene-to-supergene paragenetic sequence. Its moderate gold value (27.48 ppm), despite intense weathering, indicates partial retention of gold following sulphide breakdown rather than complete remobilisation out of the profile.

Overall, quartz is the dominant mineral phase in all samples (39–69.2 wt.%), followed by varying proportions of orthoclase and albite. Muscovite is most abundant in RR6 and RR8, indicating intense sericitic alteration, whereas clinochlore occurs principally in RR1 and RR9, reflecting chloritic alteration. Goethite is present in minor amounts (0.06–6.2 wt.%), indicating localized oxidation of iron-bearing minerals. These mineral assemblages demonstrate varying intensities of hydrothermal alteration across the study area.

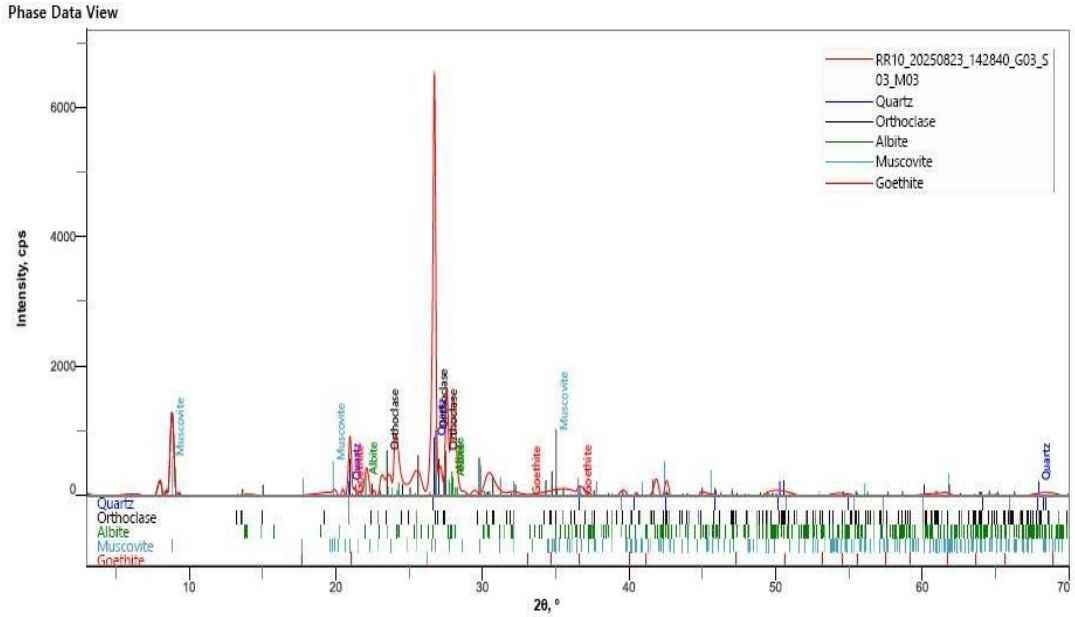

Fig. 21: XRD diffractogram of Sample RR10 obtained using Cu-Kα radiation over a 2θ range of 5–70°, with phase identification by Rietveld refinement.

Table 10: Relative Abundance of Mineral Phases Identified by XRD Analysis (RR10)

Mineral Phase	Chemical Formula	RR10 (wt.%)
Quartz	SiO_2	45
Orthoclase	$KAlSi_3O_8$	21.7
Albite	$NaAlSi_3O_8$	14.4
Muscovite	$H_2KAl_3(SiO_4)_3$	17
Goethite	FeO(OH)	2.4

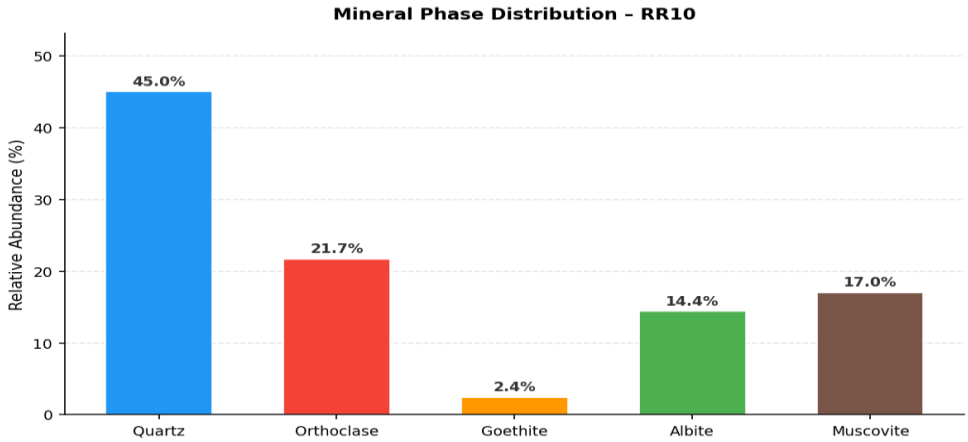

Fig. 22: Bar chart of relative mineral-phase abundance (%) for Sample RR10.

Moderate muscovite (17 wt.%) indicates measurable sericitisation, while goethite (2.4 wt.%) reflects a moderate degree of supergene oxidation, consistent with the elevated whole-rock K_2O (9.73 wt.%; Table 11) contributed by muscovite and orthoclase. The relatively high gold value (52.09 ppm) for a gneiss-hosted sample indicates that structural position at the phyllite–gneiss contact, rather than host lithology alone, exerts primary control on gold endowment. RR10 is best classified as an outer sericitic-zone sample transitional toward the chloritic margin.

Table 11. Major oxides and selected trace elements of host rock samples

Major Oxides (wt.%)	**RR1**	**RR2**	**RR3**	**RR4**	**RR5**	**RR6**	**RR7**	**RR8**	**RR9**	**RR10**
SiO_2	60.79	90.02	61.78	57.82	95.62	52.95	68.21	60.48	61.33	57.96
Al_2O_3	15.37	3.41	16.01	11.70	1.81	10.18	7.32	12.63	16.11	13.78
Fe_2O_3	12.22	2.96	11.15	9.32	0.77	12.01	18.21	7.61	11.46	8.14
CaO	2.64	0.38	2.90	6.88	0.19	7.73	0.33	6.78	2.07	6.23
K_2O	5.92	1.38	5.07	9.17	0.15	10.88	2.65	8.48	5.53	9.73
TiO_2	1.46	0.07	1.31	1.49	0.06	1.82	0.56	1.38	1.34	1.41
MnO	0.19	0.25	0.17	0.15	0.08	0.20	0.30	0.14	0.22	0.14
LOI	1.85	1.20	1.28	3.08	1.09	1.80	1.93	1.84	2.02	1.99
Trace Elements (ppm)										
Au	47.94	ND	126.24	3.35	92.73	60.39	21.85	32.34	27.48	52.09
As	ND	15	ND	23	8	ND	ND	ND	ND	ND
Cu	479	320	399	479	320	559	399	399	399	399
Pb	93	186	186	186	93	278	186	93	186	186
Zn	161	32	161	80	ND	161	80	80	161	161
Cr	889	1095	616	547	1232	958	753	547	616	479
Ni	79	79	79	79	16	79	24	79	79	79

ND = Not detected; Rock types: RR1,6,9 = Phyllite; RR2,3,5,7 = Quartz vein; RR4,8,10 = Granitic gneiss

4.2.2 Major Element Geochemistry

Major oxide data for host rocks and stream sediments are summarized in Tables 3 and 4 respectively. Silica (SiO2) dominates both datasets: host rocks range from 52.95% (RR6, phyllite) to 95.62% (RR5, quartz vein); stream sediments range from 49.21% (RSS1) to 72.76% (RSS9). The SiO_2–major oxide variation diagrams (Fig. 6) for host rocks show a clear negative correlation between SiO_2 and Fe_2O_3, CaO, and MgO, reflecting progressive depletion of ferromagnesian and carbonate

phases with increasing silicification. Alumina (Al_2O_3) shows moderate variability (1.81–16.11% in host rocks; 7.32–15.11% in river sediments), indicating differential retention of aluminosilicate phases. Fe_2O_3 is highly variable (0.77–18.21% in rocks; 2.39–33.10% in sediments), reflecting ferruginization and oxidation. K_2O ranges from 0.15% (RR5) to 10.88% (RR6), with the highest values associated with muscovite-rich phyllite and granitic gneiss.

4.4 Host Rock Gold and Pathfinder Element Geochemistry

Gold and pathfinder element data (Au, As, Cu, Pb, Zn) for the ten host rock samples are presented in Table 5. Gold concentrations range from 3.35 ppm in granitic gneiss (RR4) to 136.78 ppm in quartz vein sample RR3. Quartz vein samples consistently return the highest gold values (RR3: 126.24 ppm, RR5: 92.73 ppm, RR7: 21.85 ppm), with an exception of Sample RR2 with no detectable gold; suggested localized fluid channeling in the vein system. Among the phyllite samples, RR6 (60.39 ppm) and RR1 (47.94 ppm) are the ore-grade values, while Sample RR9 reveals 27.48 ppm (Table 3). Granitic gneiss Samples RR10 (52.09 ppm) and RR8 (32.34 ppm) also show relative elevated concentrations (Table 3). The Spatial distribution of gold and pathfinder elements in host rock samples are presented in Table 4. The concentration values of the gold and pathfinder elements follow the same trend as described for the major oxides concentration values. However, the spatial distribution maps of gold (Au) and the pathfinder elements were presented in Figs. 7-11

Table 12. Spatial distribution of gold and pathfinder elements in host rock samples

Sample	Latitude	Longitude	Au (ppm)	As (ppm)	Cu (ppm)	Pb (ppm)	Zn (ppm)
RR1	10°44′44.7″N	4°48′15.4″E	47.94	ND	479	93	161
RR2	10°45′04.5″N	4°47′54.7″E	ND	15	320	186	32
RR3	10°44′49.5″N	4°47′10.8″E	136.78	ND	399	186	161
RR4	10°45′24.5″N	4°47′30.0″E	3.35	23	479	186	80
RR5	10°46′08.0″N	4°48′05.0″E	92.73	8	320	93	ND
RR6	10°44′14.7″N	4°46′40.9″E	60.39	ND	559	278	161
RR7	10°44′22.8″N	4°46′31.8″E	21.85	ND	399	186	80
RR8	10°45′21.0″N	4°46′36.5″E	32.34	ND	399	93	80
RR9	10°45′28.1″N	4°48′10.1″E	27.48	ND	399	186	161
RR10	10°46′17.7″N	4°46′40.0″E	52.09	ND	399	186	161

ND = Not detected

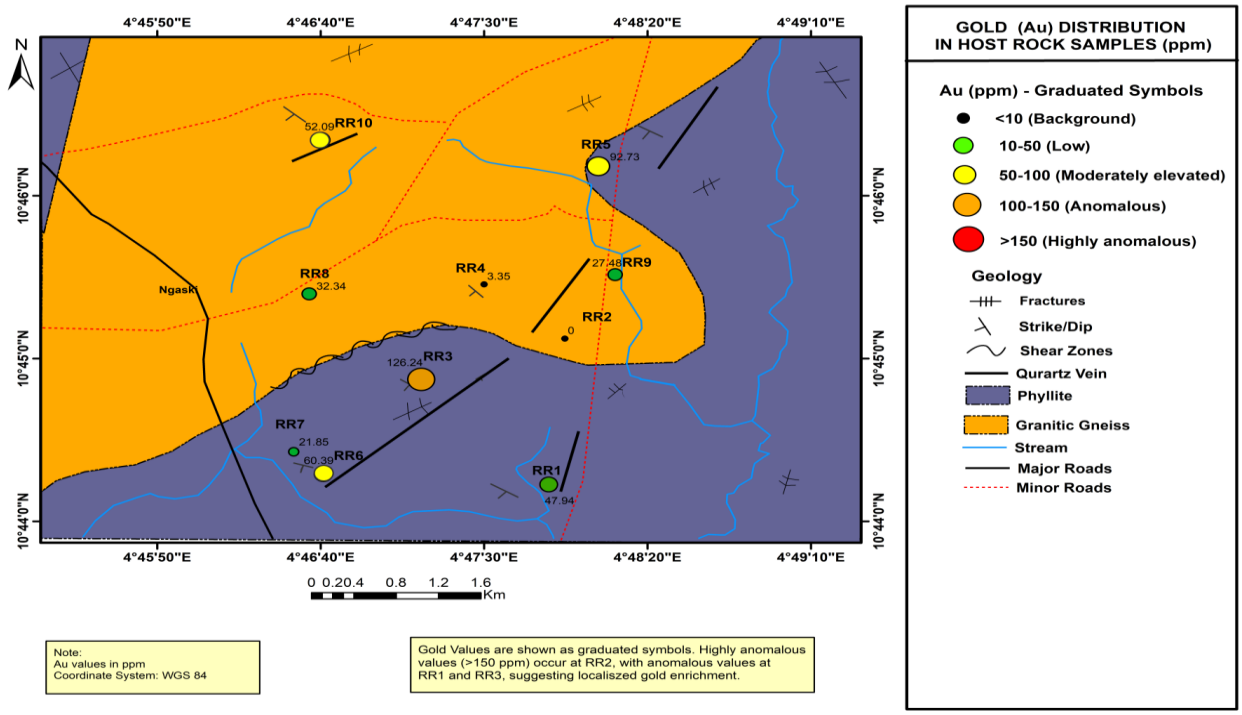

Fig. 23: Spatial distribution maps of Au in the host rocks

Gold Distribution map in host rocks show a localized anomaly concentrated along the phyllite-gneiss contact, with peak values at RR3 and evaluated atRR5. The spatial pattern aligned with mapped structures and quartz veins, indicating strong structural control on mineralization.

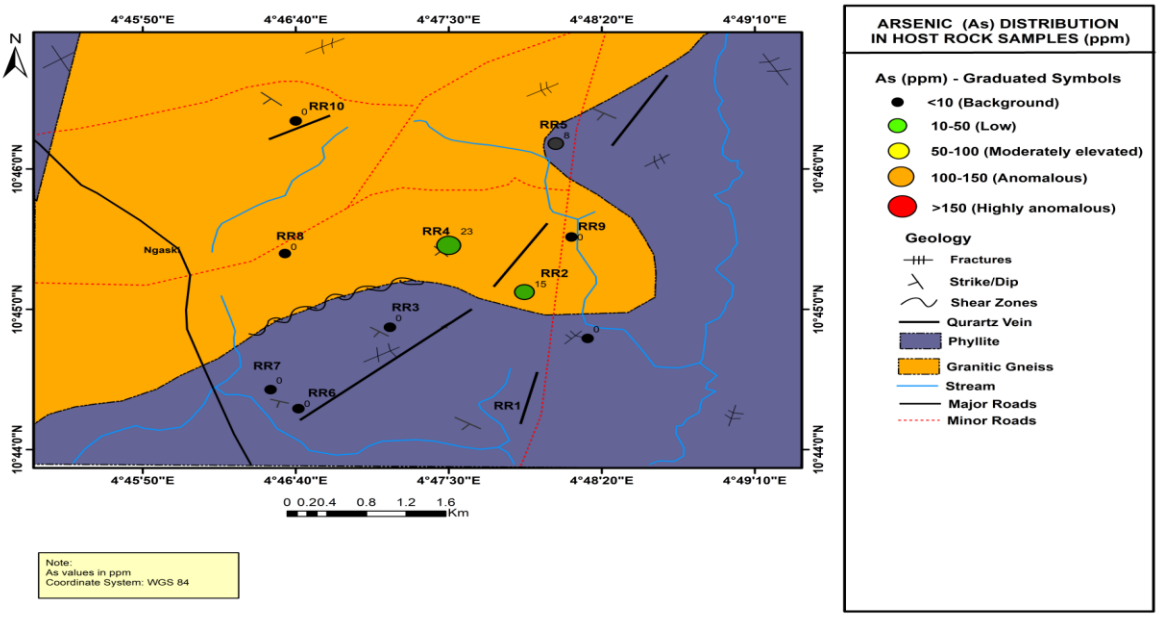

Fig. 24: Spatial distribution maps of As in the host rocks

Arsenic distribution is generally low, with slight enrichment at RR2 and RR4. The weak and scattered pattern, with limited alignment to structural features, suggests mineral arsenic association with gold mineralization in the area.

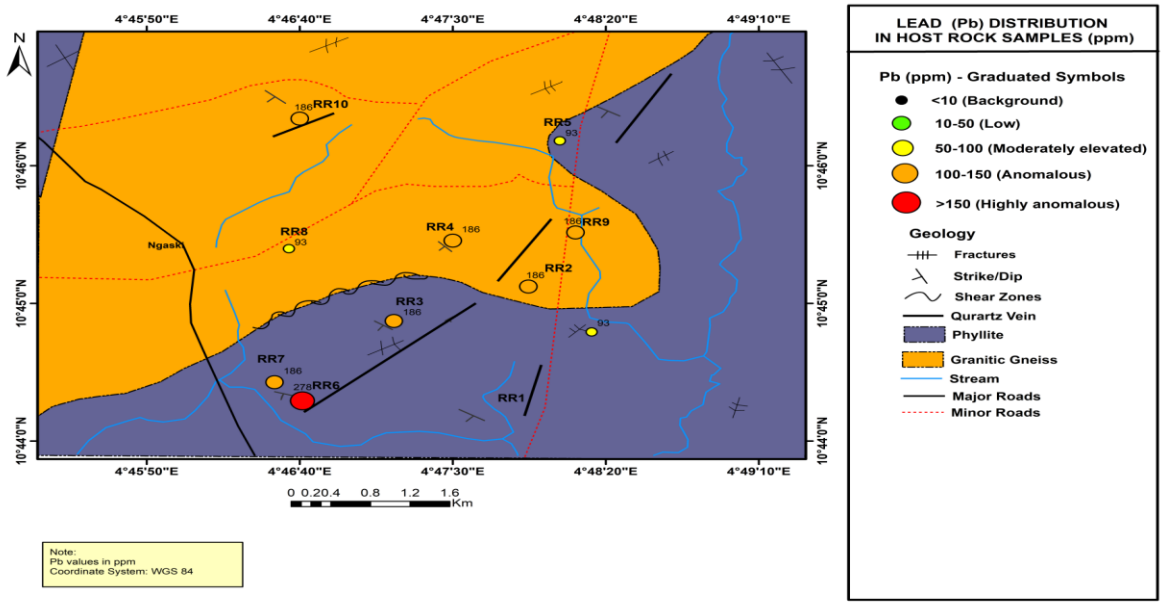

Fig. 25: Spatial distribution maps of Pb in the host rocks

Lead distribution shows moderate to high enrichment, with peak values at RR6 and elevated concentrations along the phyllite-gneiss contact. The spatial pattern suggest structural control and a possible association with mineralized zones.

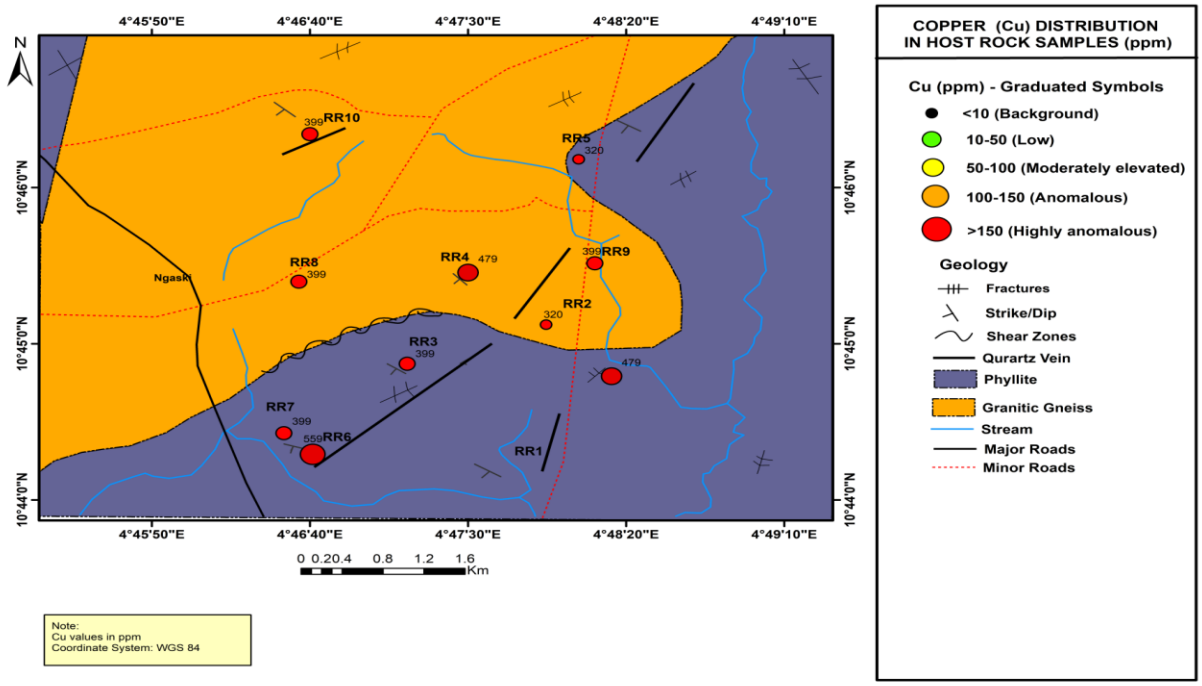

Fig. 26: Spatial distribution maps of Cu in the host rocks

Copper distribution shows strong and widespread enrichment, with peak values at RR6 and consistently high concentrations across the area. The spatial pattern. Particularly along the phyllite-gneiss contact, suggests sructual control and a clear association with the mineralized system.

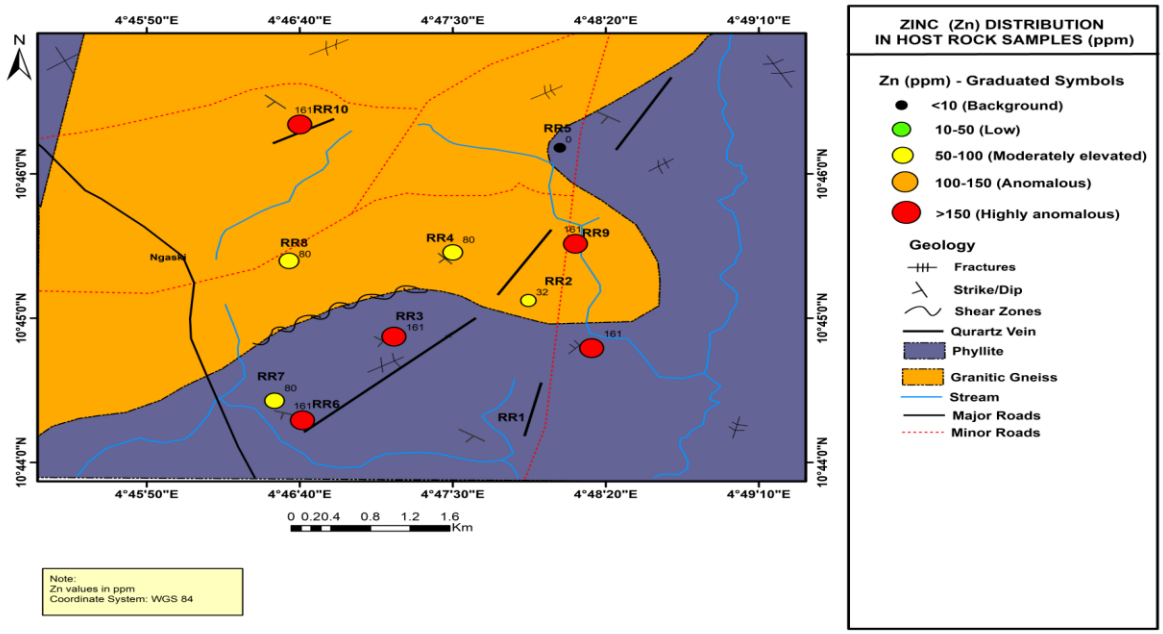

Fig. 27: Spatial distribution maps of Zn in the host rocks

Table 13. Major oxides and selected trace elements of stream sediment samples

Elemental Oxides (%)	RSS1	RSS2	RSS3	RSS4	RSS5	RSS6	RSS7	RSS8	RSS9	RSS10
SiO_2	49.21	52.55	50.85	61.13	71.55	71.89	68.21	55.45	72.76	66.54
Fe_2O_3	33.10	21.41	28.32	11.98	2.39	3.37	18.21	20.27	2.54	5.87
K_2O	2.48	5.34	3.33	8.71	8.81	9.84	2.65	5.22	11.64	11.01
Al_2O_3	10.30	15.11	13.01	12.15	12.81	10.55	7.32	11.46	8.55	10.94
MnO	1.27	1.47	1.22	0.63	0.06	0.14	0.30	0.39	0.02	0.30
Au (ppm)	122.96	216.12	129.93	18.50	20.06	ND	21.85	ND	ND	ND
Cu (ppm)	30	47	42	26	54	42	32	37	57	49
Pb (ppm)	19	45	25	22	30	23	17	40	58	19
Zn (ppm)	19	25	19	24	29	32	33	17	44	39

ND = Not detected

Table 14. Spatial distribution of gold and pathfinder elements in stream sediment samples

Sample	Latitude	Longitude	Au (ppm)	Cu (ppm)	Pb (ppm)	Zn (ppm)	Au/Cu Ratio
RSS1	10°44′08.2″N	4°47′44.3″E	122.96	30	19	19	4.10
RSS2	10°44′36.9″N	4°48′30.7″E	216.12	47	45	25	4.60
RSS3	10°44′32.0″N	4°47′50.2″E	129.93	42	25	19	3.09
RSS4	10°45′06.7″N	4°48′14.9″E	18.50	26	22	24	0.71
RSS5	10°46′08.0″N	4°46′46.6″E	20.06	54	30	29	0.37
RSS6	10°44′03.9″N	4°46′43.9″E	ND	42	23	32	—
RSS7	10°44′31.2″N	4°46′20.7″E	21.85	32	17	33	0.68
RSS8	10°45′29.0″N	4°49′03.0″E	ND	37	40	17	—
RSS9	10°45′32.9″N	4°46′17.3″E	ND	57	58	44	—
RSS10	10°46′13.6″N	4°48′15.8″E	ND	49	19	39	—

ND = Not detected; Au/Cu ratio is a dimensionless proxy for gold-dominant fluid pulses

Fig. 28: Interpolation Map of Gold Distribution within the Study Area

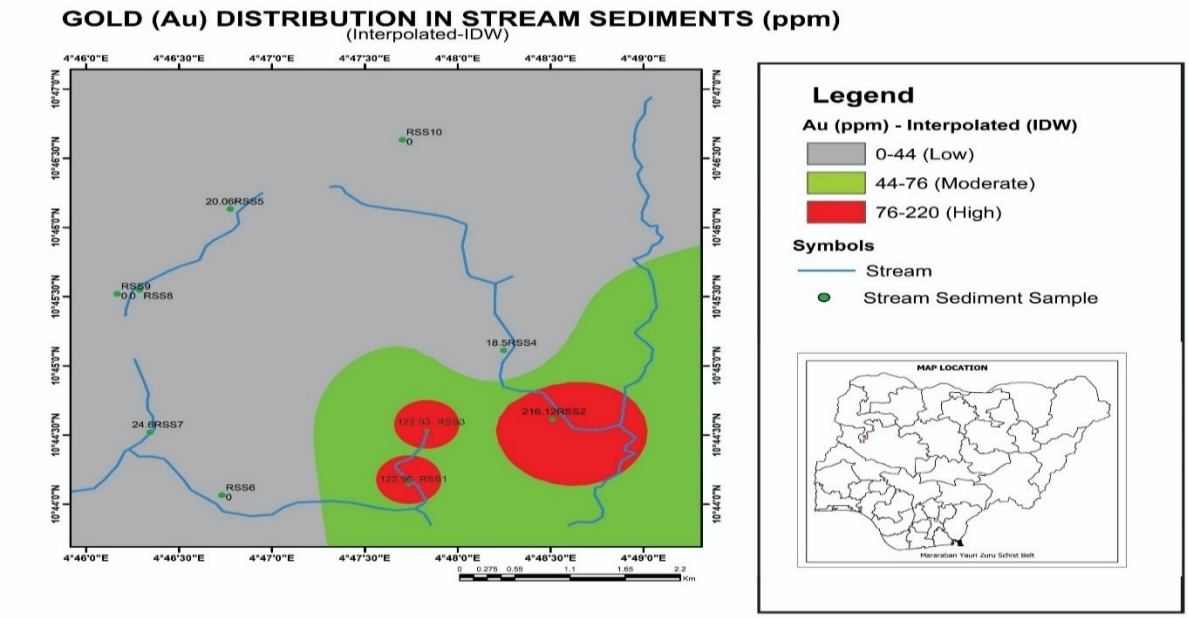

Zinc distribution shows moderate to high enrichment, with peak values at RR6,RR3, and RR9, mainly along phyllite-gneiss contact. The spatial pattern suggest structural control and partial association with the mineralized system. RSS1, RSS2, and RSS3. The parttern indicates localized gold enrichment and reflects nearby bedrock mineralization sources.

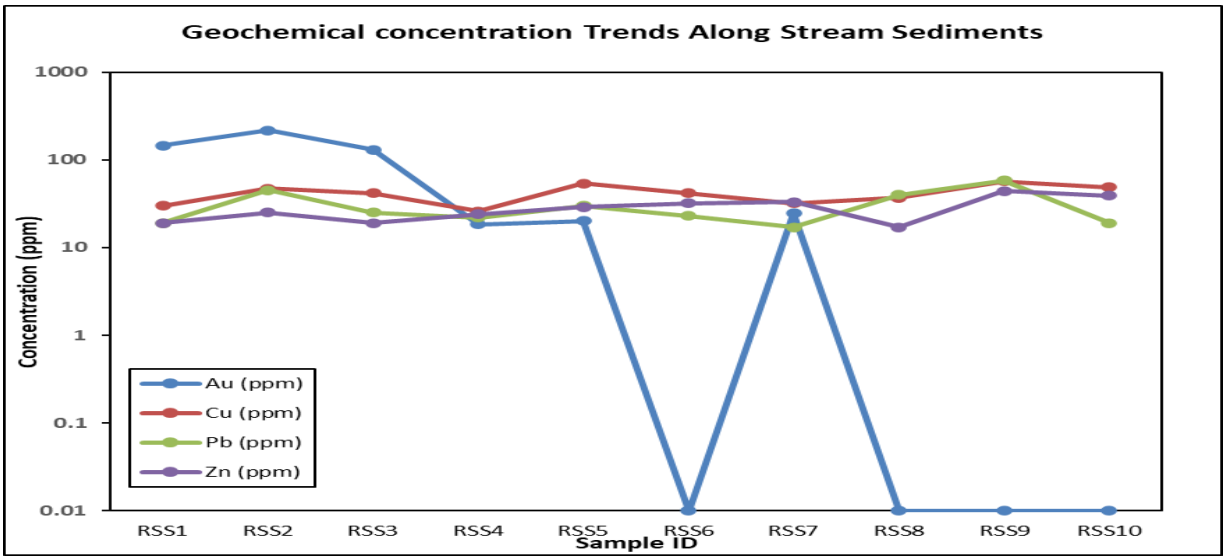

Fig.29: Geochemical Concentration Trends along Stream Sediments for Au, Cu, Pb, And Zn (In Ppm) Across Sample Points

4.5 Stream Sediment Geochemistry

Gold and trace element data for ten stream sediment samples were summarized in Tables 5 and 6, with spatial distribution shown in Figs. 12-15. Gold anomalies were recorded in six samples, with high values in Samples RSS2 (216.12 ppm), RSS3 (129.93 ppm), and RSS1 (122.96 ppm), all clustered in the southern to southeastern drainage catchments (Fig. 12).

Gold distribution in stream sediments shows distinct high-value anomalies concentrated in the southeastern sector, particularly around The geochemical trends indicate that Au exhibits strong variability, with high concentraration at RSS1-RSS3 and sharp deplection from RSS6 onword, suggesting localized gold sources and limited downstream dispwersion. In contrast, Cu,Pb,and Zn display relatively stable and consistent trends across the sampling ponts, with moderate fluctuations. The gradual increase of Cu and Zn towards RSS8-RSS10, along with localized Pb enrichment, suggests a broder and more continuous source for base metals compared to gold.

The combined petrographic, mineralogical, and geochemical datasets consistently indicate that The mean Au concentration of 88.24 ppm across anomalous samples far exceeds background values in the northern drainage sediment Samples (RSS4: 18.5 ppm and RSS5: 20.06 ppm). However, Samples RSS6, RSS8, RSS9, and RSS10 are below Au detection values; delineated at the distal section are characterized as the less-mineralized portions of the drainage system (Fig. 12).

hydrothermal alteration is closely associated with gold enrichment. Sericitization, chloritization, elevated K_2O contents, and anomalous gold concentrations collectively define the principal alteration and mineralization zones within the study area.5.0

5.0 Discussion

5.1 Hydrothermal Alteration Assemblages and Paragenetic Sequence

The combined petrographic and XRD datasets demonstrate that the original mineral assemblages of the host rocks in the Mararaban Yauri Area. *The combined petrographic and XRD datasets indicate that the primary mineral assemblages of the Mararaban Yauri host rocks have undergone varying degrees of hydrothermal alteration consistent with*

greenschist-facies conditions, in agreement with the regional structural framework reported by Riskuwa et al. (2026a). Three alteration types were identified based on evidences from XRD and thin sections which independently indicated the mineralizing system.

Sericitisation of K-feldspar is the most pervasive and the mineralogically significant alteration. Orthoclase in phyllite Samples RR6 and RR9 is distinctly cloudy under PPL. XRD data shows that Sample RR6 contain 34.0% muscovite and 25.1% residual orthoclase which indicated that the K-feldspar-to-sericite replacement is in progress , Whereas, Sample RR8 shows concentration value of 23.0% muscovite, 17.0% residual orthoclase compared with Sample RR10 with 17.0% muscovite (Table 2). The consistent co-occurrence of residual orthoclase and secondary sericite across multiple samples suggests progressive hydrolysis of K-feldspar by infiltrating hydrothermal fluids. *This mineral assemblage is consistent with hydrothermal alteration associated with cooling and fluid–rock interaction.* This sericitisation pattern defines the inner alteration zone of the hydrothermal system and is diagnostic of the sericitic alteration halo, the main characteristic of orogenic gold deposits worldwide (Zhou et al., 2022; Mao et al., 2024). Importantly, the muscovite-rich zones in Samples RR6 and RR8, spatially coincide with the highest gold recovery samples, affirms sericitisation as the most reliable mineralogical vector towards ore-grade mineralization in the study area. This assertion had been established by Abdullahi et al. (2022) for the broader Zuru schist belt, also by Garba (2003) for other Nigerian schist belts gold systems.

Chloritisation of biotite represents a secondary hydrothermal alteration assemblage that marks the propylitic margin of the hydrothermal system. In Samples RR1 and RR9, chlorite replaced biotite along grain boundaries and cleavage planes, identifiable by anomalous blue interference colours under XPL (Plate 2). XRD data further confirm the volumetric significance of this replacement where Samples RR1 and RR9 contain 19.0% and 12.0% clinochlore and biotite diminished respectively. Chloritisation in orogenic gold systems reflects the low- to medium-temperature conditions at the outer margins of the hydrothermal envelope, where the incoming hydrothermal fluid reacts with mafic minerals at temperatures typically below 300°C (Deng et al., 2020).

The spatial distribution of chlorite-bearing samples (RR1 and RR9) at the periphery of the high-gold anomaly corridor, flanking the sericite-dominant core samples (RR6, RR8), is consistent with lateral alteration zonation of an orogenic gold system- sericitic core → propylitic margin. This zonation provides a mineralogical vector for locating the highest-grade ore zones. *These alteration patterns may provide useful mineralogical vectors for future exploration targeting.* (Deng et al., 2020; Fagbohun et al., 2020).

Supergene oxidation expressed as goethite in five samples (RR9: 6.2%; RR4: 4.1%; RR1: 3.4%; RR10: 2.4%; RR7: 1.0%), provides geochemically significant evidence for earlier hypogene sulphide mineralization (Table 2).Goethite in the study area is interpreted to have formed predominantly through supergene oxidation of iron-bearing sulfides**.** It forms exclusively through the oxidation of iron sulphides, such as pyrite or arsenopyrite, during near-surface weathering. Petrographically, anhedral opaque minerals which align along foliation planes in phyllite and quartz vein samples are interpreted to represent altered primary sulfide minerals. (pyrite, arsenopyrite), subsequently converted to a stable goethite mineral during tropical weathering. This interpretation correlates with the detection of arsenic in Samples RR2 (15 ppm), RR4 (23 ppm), and RR5 (8 ppm) (Table 5). This implies that arsenopyrite probably co-exist with sulphide phase. Goethite halos in

weathered orogenic gold systems are established proximity indicators for primary Au-bearing sulphide assemblages at depth (Cave et al., 2023). The elevated Fe_2O_3 in stream sediment Samples RSS1 (33.1%) and RSS3 (28.32%) independently confirms the oxidation of primary sulphide phases in the upstream bedrock. This observation provides additional support for the interpretation of hypogene sulfide mineralization for hypogene sulphide mineralization. The combined alteration assemblage of quartz, muscovite (sericite), clinochlore, and goethite after sulphide suggests greenschist-facies hydrothermal alteration in a structurally controlled orogenic gold system (Groves et al., 1998; Abdullahi et al., 2022; Garba, 2003).

5.2 Geochemical Controls on Gold Distribution and Pathfinder Signatures

The extreme silica enrichment in quartz vein Samples RR5 (95.62% SiO_2) and RR2 (90.02% SiO_2) reflects repeated influx of silica-saturated hydrothermal fluids along structurally controlled fractures and shear zones (Garba, 2003; Groves et al., 1998). The inverse relationship between SiO_2 and Fe_2O_3, CaO, and MgO in the variation diagrams (Fig. 6) reflects the progressive leaching of ferromagnesian and carbonate phases during silicification, consistent with felsic source rocks undergoing both hydrothermal alteration and tropical weathering. This trend is characteristic of silicification associated with orogenic gold systems in the Nigerian Basement Complex (Garba, 2003; Okonkwo et al., 2021).

The spatial distribution of gold in host rocks (Table 5; Fig. 7) defines a coherent NNW–SSE mineralized corridor: RR3 (126.24 ppm, quartz vein), RR5 (92.73 ppm, quartz vein), RR6 (60.39 ppm, phyllite), RR10 (52.09 ppm, granitic gneiss), RR1 (47.94 ppm, phyllite), RR8 (32.34 ppm, granitic gneiss), and RR9 (27.48 ppm, phyllite). The highest gold values are found in quartz vein Samples (RR3 and RR5), agreeing that the veins are the principal ore structures. The rheological contrast between phyllite and granitic gneiss generated a mechanically heterogeneous zone that focused dilatancy, enhanced fracture permeability, and channelled hydrothermal fluid flow, creating the conditions for gold precipitation in the structural interface.

The pathfinder element patterns add important nuance to the gold distribution picture. Copper (320–559 ppm) is elevated uniformly across all lithological units and rock types, with no systematic spatial association with the gold-anomalous samples. This suggests that Cu in the Mararaban Yauri area is a background geochemical characteristic of the Zuru Schist Belt terrain rather than a direct gold indicator in this particular sample suite. Lead (93–278 ppm) follows a broadly similar diffuse pattern, with the highest value in Sample RR6 (278 ppm), a phyllite sample that also carries high gold (60.39 ppm). Zinc shows a notable pattern with Sample RR5 having the second-highest gold concentration value (92.73 ppm), and zero detectable zinc; others have high-gold concentration values with 80–161 ppm of Zn. The decoupling of Au and Zn in Sample RR5 plausibly reflects a gold-dominant fluid pulse with a distinct base-metal-depleted chemistry; possibly represents a subsequent gold-richer fluid event superimposed on an earlier Cu–Pb–Zn mineralized episode within the same structural corridor. Arsenic is geochemically focused (detected only in RR2, RR4, RR5) and does not co-vary systematically with gold, possibly because the original arsenopyrite has been remobilized during weathering. These observations collectively suggest two partially separate hydrothermal events or fluid compositions, operated within the same NE–SW structural framework in comparable with Nigerian schist belt systems (Garba, 2003 and Abdullahi et al., 2022), also in analogous to West African orogenic settings (Goldfarb et al., 2001).

5.3 Stream Sediment Geochemistry as an Exploration Tool

The spatial clustering of the highest concentration values of stream sediment gold anomalies in Samples RSS2 (216.12 ppm), RSS3 (129.93 ppm), and RSS1 (122.96 ppm) in the southern drainage catchment area correlate with downstream locations of the host rock anomaly corridor. This corroborates the bedrock gold source and stream sediment geochemistry as an effective first-pass reconnaissance tool for shiest belt gold investigation (Fig. 8; Table 6). The downstream concentration trend in Figure 9 shows high Au values in the proximal-to-mid-channel positions, declining progressively toward distal samples locations. This trend is consistent with the limited hydrodynamic mobility of gold due to its high density. This gold dispersal pattern contrasts the more diffuse downstream concentrations distributions of Cu, Pb, and Zn which reflect higher aqueous mobility under tropical weathering conditions. The high Au/Cu ratios at the most anomalous stream sediment sites (RSS2: 4.60; RSS1: 4.10; Table 6) further indicates gold-dominant fluid conditions in the upstream bedrock source area. These patterns are comparable to stream sediment gold dispersal in the Birnin Yauri schist belt (Ola et al., 2022) and in the Zuru Schist Belt (Fagbohun et al., 2020), reemphasizing the applicable of stream sediment geochemistry as a tool in this geological setting investigation.

5.4 Genetic Model for Gold Mineralization

The integrated petrographic, XRD, and XRF datasets indicate that gold mineralization within the Mararaban Yauri area is structurally controlled and associated with hydrothermal fluids that migrated along NE–SW-oriented shear zones and quartz-vein systems during the Pan-African Orogeny. Hydrothermal alteration is characterized by progressive sericitization and chloritization, accompanied by localized silicification and subsequent supergene oxidation of sulfide minerals. The spatial coincidence of intense sericitic alteration, elevated K_2O contents, quartz veining, and anomalous gold concentrations suggests that the most prospective zones occur where structurally controlled fluid flow intersected chemically reactive host rocks. The stream-sediment geochemistry further confirms the presence of upstream mineralized bedrock sources and demonstrates the effectiveness of drainage geochemistry for regional exploration within the Zuru Schist Belt.

6.0 Conclusion

This study presents an integrated mineralogical and geochemical characterization of gold-bearing rocks and stream sediments from the Mararaban Yauri area of the Zuru Schist Belt, northwestern Nigeria, using petrography, X-ray diffraction (XRD), and X-ray fluorescence (XRF). The results demonstrate that gold mineralization is structurally controlled, occurring mainly within quartz veins hosted by phyllite and granitic gneiss, and is associated with characteristic hydrothermal alteration assemblages. The integration of petrographic, mineralogical, and geochemical data has improved the understanding of the alteration processes, fluid–rock interactions, and controls on gold mineralization within the study area.

Petrographic and XRD analyses identified quartz, feldspars, muscovite, chlorite, biotite, garnet, hornblende, and goethite as the principal mineral phases. Quartz is the dominant mineral in all samples, while the distribution of muscovite, chlorite, and goethite indicates well-developed sericitic, chloritic, and supergene alteration. Sericitization represents the dominant hydrothermal alteration process and is closely associated with elevated K_2O contents and higher gold concentrations, whereas chloritization characterizes the outer alteration zones. The occurrence of goethite reflects oxidation of earlier sulfide minerals during weathering and supports the interpretation of a greenschist-facies hydrothermal system related to the Pan-African Orogeny.

Whole-rock geochemistry shows significant silica enrichment in quartz veins, reflecting intense silicification, while decreasing Fe_2O_3, CaO, and MgO contents indicate progressive alteration of ferromagnesian minerals. Gold concentrations vary considerably, with the highest values occurring in quartz veins and along the phyllite–gneiss contact, demonstrating that structural controls played a greater role in ore localization than host lithology alone. Copper and lead are widely distributed, whereas arsenic shows localized enrichment and appears to be a secondary pathfinder element within the mineralizing system.

Stream sediment geochemistry successfully delineated anomalous gold concentrations that correspond closely with upstream mineralized bedrock, confirming the effectiveness of drainage geochemistry as a reconnaissance exploration tool. The highest gold anomalies occur within the southern drainage catchments, while Cu, Pb, and Zn display broader dispersion patterns consistent with their greater mobility during weathering.

The integrated mineralogical and geochemical evidence indicates that gold mineralization in the Mararaban Yauri area formed from hydrothermal fluids migrating along NE–SW-trending shear zones and quartz veins during the Pan-African Orogeny. Fluid–rock interaction produced silicification, sericitization, chloritization, and localized sulfide mineralization, followed by supergene oxidation. The close spatial association between hydrothermal alteration, quartz veining, and elevated gold concentrations provides reliable exploration vectors for identifying additional mineralized zones.

Overall, this study provides a comprehensive mineralogical and geochemical framework for understanding gold mineralization in the Mararaban Yauri segment of the Zuru Schist Belt. The findings contribute to the knowledge of orogenic gold systems within the Nigerian Basement Complex and provide valuable exploration criteria for future mineral resource evaluation in the study area and similar Precambrian terranes.

Acknowledgements

The authors acknowledge Nasarawa State University Keffi and Federal University Birnin Kebbi for institutional support. Laboratory facilities and analytical instruments were provided by the National Steel Raw Materials and Exploration Agency (NSRMEA), Kaduna. The Ministry of Solid Mineral Development, Kebbi State, provided field equipment. Financial support was provided by Alhaji Sofiu Alasinri Saka and Alhaji Ibrahim Ahmed Suru. The authors thank the Mararaban Yauri community for permission to conduct fieldwork and sample collection.

7.0 References

Abdullahi, U., Garba, I., & Ismail, A. Y. (2022). Hydrothermal alteration and gold mineralization in parts of the Zuru Schist Belt, northwestern Nigeria. Journal of African Earth Sciences, 186, 104423.

Cave, B. J., Lilly, R., & Barovich, K. (2023). Goethite as a geochemical vector to gold mineralization in weathered orogenic gold systems. Economic Geology, 118(3), 591–612.

Deng, J., Wang, Q., & Wan, L. (2020). Propylitic alteration patterns in orogenic gold deposits: Implications for fluid flow pathways and exploration targeting. Ore Geology Reviews, 123, 103598.

Fagbohun, B. J., Omitogun, A. A., & Salako, K. A. (2020). Pathfinder element geochemistry in the Zuru Schist Belt, northwestern Nigeria. Journal of Geochemical Exploration, 211, 106469.

Garba, I. (2000). Origin of Pan-African mesothermal gold mineralisation at Bin Yauri, Nigeria. Journal of African Earth Sciences, 30(3), 593–605.

Garba, I. (2003). Geochemical discrimination of newly discovered rare-metal bearing

and barren pegmatites in the Pan-African ~600 Ma Basement of northern Nigeria. Applied Earth Science, 112(3), 287–292.

Goldfarb, R. J., Groves, D. I., & Gardoll, S. (2001). Orogenic gold and geologic time: A global synthesis. Ore Geology Reviews, 18(1–2), 1–75.

Groves, D. I., Goldfarb, R. J., Gebre-Mariam, M., Hagemann, S. G., & Robert, F. (1998). Orogenic gold deposits: A proposed classification in the context of their crustal distribution and relationship to other gold deposit types. Ore Geology Reviews, 13(1–5), 7–27.

Mao, J., Chen, M., Yuan, S., & Guo, C. (2024). Feldspar hydrolysis in hydrothermal gold systems: Petrographic and geochemical constraints from Precambrian terrains. Geoscience Frontiers, 15(1), 101546.

Okonkwo, C. T., Arabi, A. S., & Shehu, S. A. (2021). Gold mineralization in the Precambrian basement of Nigeria: A review. Journal of African Earth Sciences, 175, 104094.

Ola, P. S., Adekola, S. A., & Ogunyele, A. C. (2022). Stream sediment and rock geochemistry of the Birnin Yauri schist belt gold mineralization, northwestern Nigeria. Geochemistry, 82(4), 125915.

Zhou, T., Zhang, L., & Fan, Y. (2022). Sericitic alteration halos in orogenic gold systems: Petrographic and geochemical constraints. Mineralium Deposita, 57(2), 319–338.

Declarations

Ethical Approval and Consent to Participate

Not applicable

Consent for Publication

Not applicable.

Availability of Data and Materials

The data supporting the findings of this study are available from the corresponding author upon reasonable request.

Competing Interests

The authors declare that they have no competing interests.

Funding

The authors received no specific grant from any funding agency in the public, commercial, or not-for-profit sectors for the conduct of this study.

Authors' Contributions

Samaila Garba Riskuwa conceived the study, conducted field investigations, collected samples, performed laboratory analyses, interpreted the mineralogical and geochemical data, and drafted the manuscript. Ishak Yau Tanko supervised the research, contributed to the study design, validated the analytical results, critically reviewed and revised the manuscript, and approved the final version for publication. Both authors read and approved the final manuscript.

Publisher's Note

The authors are solely responsible for the content of this manuscript. The publisher remains neutral with regard to jurisdictional claims in published maps and institutional affiliations.